FINAL TECHNICAL REPORT

NSF Project ATM 7820149

Aircraft Measurements of Aerosol Optical Properties During the MONEX Program.

by

E. M. Patterson, G. W. Grams, and C. O. Pollard

School of Geophysical Sciences
Georgia Institute of Technology
Atlanta GA 30332

MARCH 1983

EXECUTIVE SUMMARY

One of the primary scientific objectives of the 1979 Summer MONEX program was the study of the effects of heat sources on the monsoon circulation. To meet this objective, MONEX included an extensive set of radiation measurements from aircraft, ground stations and ships. These measurements included measurements on the NASA CV-990 that had the objective of defining heat sources over Saudi Arabia, India, and adjacent ocean areas during the Arabian Sea portion of the MONEX experiment. Aerosol measurements during these flights, and during selected NCAR Electra flights, provided the opportunity to determine aerosol concentrations and radiative properties for parameterization and interpretation of in-situ and satellite based radiation measurements. As part of the Georgia Tech participation we collected aerosol samples aboard the aircraft on flights over Saudi Arabia, India and the Arabian Sea. These samples were subsequently analyzed to determine aerosol mass concentration, composition and mineralogy, real and imaginary components of the refractive index, and particle size distribution. We also used the aerosol data, together with concurrent aircraft observations, to make radiation transfer calculations for comparison with simultaneous radiation measurements by other experimenters.

Our aerosol mass concentrations were determined gravimetrically. The most notable feature of these concentration data is the high measured concentration within the haze layer, ranging up to more than 750 $\mu g/m^3$. Geometric mean concentration values within the haze layer were calculated to be 280 ppbm over Saudi Arabia, 150 ppbm over India and 240 ppbm over the Arabian Sea. The high altitude data also indicated high concentration within the MONEX area. These mass concentrations measured by us within the haze layer appeared to be significantly lower than those measured simultaneously by PMS optical particle counters.

Size distributions determined by SEM analysis of Nuclepore Filters show the dominance of soil-derived particles. Although our CV-990 low volume collection apparatus has reduced collection efficiency for particles larger than 1 μm radius, our size distribution analysis indicates that the aerosols over India, Saudi Arabia, and adjacent oceanic regions have sizes that are quite similar to those measured previously for such soil-derived particles. There were indications, as well, of the presence of particles smaller than the soil particles that would have little or no effect on total mass, but could have some minor effect on the radiative properties. Optical microscopic analysis of selected high-volume filters showed a greater variation in composition than seen in our earlier Saharan measurements due to the larger number of sources for these MONEX aerosols and the greater proximity to these sources. No separate population of highly absorbing small particles was seen.

Optical properties measured for these aerosols showed n_{RE} (real component of refractive index) values near 1.6 for this data set. n_{IM} (imaginary component of refractive index - an absorption parameter) values showed more variation. All of the values measured within the haze layers were in the range expected for soil-derived aerosols. Measurements of n_{IM} over the Rub'al Khali desert showed values near .004 between 500 and 700 nm, with slightly higher values measured at shorter wavelengths. Other measurements within the haze layer show the same qualitative character, with 500 nm values ranging between $\sim$ .014 and .002. Measurements above the main haze layers show more variation in measured absorption; in some cases, surprisingly high values of n_{IM} were measured. We were able, in some cases, to relate our aerosol samples to specific source regions.

We used our measured aerosol properties to calculate the overall extinction, scattering and absorption for these aerosols. We then used these calcula-

ted radiative properties as well as indirect inferences of aerosol optical depth to calculate spectral reflectance and radiation divergences within the haze layer using a delta Eddington radiation transfer routine. These calculated spectral reflectances were consistent with TIROS-N determinations discussed by Ackerman and Cox. This comparison indicates an ω (the ratio of aerosol scattering to aerosol extinction) of somewhat less than 0.9 in the wavelength band between 0.55 and 0.9 μm. Our radiative transfer calculations indicate significant *in-situ* heating averaging $\sim$ 0.2°C/hour in the haze layer at local noon, due to the absorption of short wave solar radiation. A further comparison of calculated radiative divergence, parameterized as a functional absorption, with that measured by Ackerman and Cox, however, shows some inconsistancy in the two data sets. Our inferred values of ω between 0.8 and .9 predict considerably more radiation divergence than actually measured. The measured divergences are consistent with an ω of 0.96. The reason for the discrepancy is not known at this time.

INTRODUCTION

A monsoon subprogram was developed within the framework of the Global Atmospheric Research Program; this subprogram consisted of a coordinated group of observational efforts, together with associated data processing and research programs. The central field experiment of the monsoon subprogram was the Monsoon Experiment (MONEX), which included observational studies during the period of the first GARP Global Experiment (FGGE) over the Arabian Sea, Indian Ocean, Bay of Bengal, and Southeast Asia. MONEX had as one of its primary scientific objectives a study of the effects of heat sources on the monsoon circulation (ICSU/WMO, 1976). To meet this scientific objective, MONEX included an extensive set of radiation measurements from aircraft, ground stations, and ships, including measurements on the NASA CV-990 that had the objective of defining the heat sources over selected areas of Saudi Arabia, India and adjacent ocean areas during the Arabian Sea experiment. These aircraft flights also provided the opportunity for determining aerosol concentrations and radiative properties for parameterization and interpretation of the in-situ radiation measurements as well as satellite remote sensing data.

These aircraft measurements provided an extensive set of aerosol data that is a valuable addition to the global data base for geophysical studies of aerosol climatology. These aerosol measurements include the optical property data complementary to the radiation measurements. Comparisons between the aerosol and the radiation measurements have shown areas of agreement as well as disagreement. In the following sections, we will discuss the experimental procedures; mass concentration data; the composition, mineralogy and real refractive index measurements; particle size distribution measurements; and absorption (imgginary refractive index component) measurements. We will also discuss some of our overall aerosol results in relation to concurrent radiation measurements.

EXPERIMENTAL PROCEDURES

The aerosol samples were collected aboard the NASA CV-990 during the 1979 Summer MONEX program. The sampling system for this experiment consisted of a high volume sampler and a low volume sampling system. The high volume system consisted of a 5 cm diameter inlet tube, an expansion chamber designed to produce maximum flow through the system, which provided a transition between the inlet tubing and a 25 cm diameter filter holder. Behind the filter, the sampling line consisted of flexible tubing leading to a 5 cm exhaust tube. The pressure drop (ΔP) across the filter was due to air stagnation in the sampler ($\sim$ 80% of ΔP) as well as pressure reduction below ambient at the exhaust port ($\sim$ 20% of ΔP). The system provided a flow of $\sim$ 130 m^3/hr through a 25 cm Delbag fibrous polystyrene filter.

The low volume filter system consisted of 2.5 cm inlet tubes which were expnaded into 5 cm manifold tubes. Secondary flow pick-offs from these manifold tubes provided air flow for the low volume samples which were operated at flows of $\sim$ 10-15 $\ell\ m^{-1}$. Any of various filter types could be used in the system; the standard filters used were 0.4 μm pore size Nuclepore filters.

The aircraft missions during MONEX included both flight legs above the haze layers (high altitude flights, generally at altitudes of 10-12 km) and flight legs within the haze layers. There were, in addition, ferry flights from the aircraft base to the measurement locations. [Detailed flight patterns are shown in Smith et al., 1980]. These flight sequences afforded the opportunity for sampling both above and within the haze layer. The general area of the measurements is shown in Fig. 1, which we have adapted from Smith et al. (1980). The CV-990 was initially based in Dhahran, Saudi Arabia with research flights over the "Empty Quqrter" - the Rub'al Khali desert area of Saudi Arabia and adjacent areas of the

Arabian Sea. The CV-990 was then based in Bombay, India and research missions were flown over India and the Arabian Sea. Both within-haze and high altitude samples were collected in each of these regions. Specific areas of these flights are discussed below.

Sampling times for the within-haze samples were limited to periods of a few minutes to $\sim$ 30 minutes; due to the high aerosol concentrations present, these short sampling times were adequate for our collection. Sampling times at the higher altitudes were much longer, due to the lower concentration of aerosols. In some cases, the sampling time for one sample included two day's flight operations.

The subsequent analysis of the filters was performed in our laboratories. Aerosol concentrations were determined gravimetrically using the high volume aerosol samples. In this procedure the Delbag filter and collected aerosol material is dissolved in an organic solvent. The aerosol material is sedimented out of suspension, and the dissolved filter material is removed by repeated washing with the solvent. The solvent is then removed by evaporation and the aerosol residue is weighed. From the mass of aerosol and the known volume of air through the filter, the mass concentration of the aerosol was determined.

A portion of this material was analyzed to determine the absorption parameter, expressed as the imaginary component of the refractive index, by means of diffuse reflectance measurements (Patterson et al., 1977; Patterson and Marshall, 1982). The diffuse reflectance measurements were made for all of our samples for which adequate material was obtained.

Selected samples, generally samples collected within the haze layers for which concentrations were high, were analyzed by optical microscopy to determine the sample mineralogy, and the real component of the refractive index. Selected

samples were also examined by scanning electron microscopic (SEM) analysis to estimate particle size distribuitons.

In addition, data was analyzed for one haze layer flight aboard the NCAR Electra aircraft for a complete case study of aerosol size and optical properties.

CONCENTRATION DATA

Aerosol mass concentrations were determined gravimetrically as discussed above. These data are expressed both as ambient volume concentrations and as mass mixing ratios. Such concentrations were determined for both high-altitude and within-haze layer samples. The high-altitude samples were collected at altitudes of more than 9 km; those from within the haze layers at altitudes between the surface and the top of haze layers, at altitudes of less than 5 km.

The ambient concentration data calculated from our aerosol mass measurements are shown in Table I (within haze layer) and in Table II (above haze layer).

The most notable feature of these concentration data is the high concentration within the haze layer. Our measured concentrations range up to more than 750 $\mu g/m^3$. Averages shown in Table III show geometric mean values within the haze layer of 280 ppbm over Saudi Arabia, of 150 ppbm over India and of 240 ppbm over the Arabian Sea. Although these mean values cannot be taken as long term concentration averages, they do indicate the very large concentrations that can be observed in this region.

Similarly, the high altitude data also indicate high concentrations. This is perhaps not surprising in the MONEX area, but the relatively high measured concentrations outside of the MONEX study measured during the ferry flights were somewhat surprising to us.

SIZE DISTRIBUTION MEASUREMENTS

Particle sizes were determined from an analysis of SEM photographs for selected low-volume samples. Two photomicrographs for the low level (0.3 km) sample of Flight 8 are shown in Figs. 2a and 2b. The larger particles shown in 2a are the soil particles. These particles range in size between $\sim$ 0.4 μm radius and 6 μm radius. These sizes are smaller than we observed in our high volume samples due to a reduced sampling efficiency for particles with $r > 1$ μm for the low volume sampling system. This collection efficiency reduction is similar to that discussed by Patterson et al. (1980).

There is also a population of smaller particles that appear to be amorphous, almost spherical, in form, without the structure associated with the larger soil particles. The source of these smaller particles is not known. Elemental analysys with the SEM X-ray fluorescence apparatus shows that these particles contain both the S and Si, suggesting that soil particles could have served as nuclei for sulfate formation.

A dN/d log r plot of this size distribution is shown in Fig. 3; the amorphous particles make up the smaller particle mode in this figure. The circles are actual measured dN/d log r values. Values measured independently from individual photographs have resulted in some independent values of dN/d log r at a given radius (such as those at $\sim$ 0.3 μm and 3 μm). This consistancy in such independent points provide an indication of the accuracy and precision of sizing procedures; for these results, there appears to be reasonably good agreement. The solid line is not a best fit line- but is provided as an approximation for better visualization of the size distributions. The break point between the modes is at the radius value that marks the transition between the two classes of particles.

This approximation has been used to calculate the volume distribution (-+-+-+) shown in Fig. 4. This figure also shows the simultaneous size distribution reported by Ackerman and Cox (1982), [their 0.3 km Flight 8 data] as a solid line. It is apparent in this figure that the total measured volume associated with the smaller particles is much less than that asosciated with the larger soil particles ($\sim$ 9 $\mu m/^3cm^3$ compared with 63 $\mu m^3/cm^3$).

It is also apparent that our measured volume distribution shows some significant differences from that measured by Ackerman and Cox. The Ackerman and Cox distribution does not extend to small enough sizes to define a small particle mode; and their distribution shows considerably more volume in the mode between 1 and 10 μm radius (with larger mean size) than do ours. The differences in the large particle mode are at least partially due to the fact that our sampling efficiencies are less than 1 for supermicron particles. Because of this reduced sampling efficiency with larger sizes, we would expect the actual dN/d log r maximum to be shifted to a somewhat larger radius and for the total volume to be larger than that inferred from our SEM data. As a comparison, the mass concentration inferred for these soil-derived particles is $\sim$ 150 $\mu g/m^3$ (assuming a specific gravity of 2.5). The mass concentration inferred for our simultaneous high volume sample is 530 $\mu g/m^3$; while that inferred by Ackerman and Cox from their data is $\sim$ 3200 $\mu g/m^3$. These larger concentration values are considered to be more representative of the actual concentration than our smaller SEM values. The possible importance of this smaller particle mode, for aerosol optical properties as well as a comparison of these concentration measurements will be discussed later.

Other measurements over India do not show this small particle population. For example, the low level measurements from Flight 15, shown in Fig. 5a and 5b show only the usual soil particles. High altitude measurements on this and other

flights showed particle concentrations that were too low to determine detailed size distributions. Filters collected over India at high altitudes do suggest, however, that the soil particles are the major component of the aerosol.

Other size distribution measurements made over the Arabian Sea from optical particle size instrumentation aboard the NCAR Electra aircraft are shown in Fig. 6. These data are from optical probes both internal and external to the aircraft and should be representative of the actual size distribution without any bias due to air sampling procedures. These data show a volume distribution with the maximum size at $\sim$ 2 μm radius. No bimodal structure is seen on this distribution, although it cannot be conclusively ruled out. These Electra data show distributions that are qualitatively similar above and within the haze layer, although total concentrations decrease with altitude as in the Indian data and the Saudi Arabian data.

In general, these data confirm the picture of a soil aerosol having predictable size distributon. Close to aerosol sources, our data show a volume mean radius (r_v) of at least 2 μm. Equivalent data of Ackerman and Cox show a r_v of $\sim$ 7 μm. Eaelier data collected over India (Peterson, 1968) discussed by Patterson and Gillette (1977) show an r_v of $\approx$ 4 μm. The Ackerman and Cox data show hints of a particle mode, a soil characteristic mode whose presence is confirmed by our high volume samples. The Arabian Sea samples show a decrease in mode size, as expected due to the greater time during which the particles have been airborne.

COMPOSITION

The mineralogical composition and refractive index (n_{RE}) of these samples were determined by means of optical microscopic analysis. Refractive indices were determined using variable index immersion oils by means of the Becke line technique (Patterson et al., 1977). The mineralogy was determined on the basis of sample appearance under polarized and unpolarized light as well as by means of the measured refractive indices. Estimates of the mineral composition and values of the refractive indices for each of these components are shown in Table IV for each of these selected samples. The general sampling region in which the sample was collected is also given.

The samples analyzed by optical microscopy have a mass that is composed almost entirely of mineralogical components. Any small non-mineral component, such as that seen in the small particle mode of Fig. 3, represents only a small fraction of the sample. In addition, any non-mineral component will be composed of particles at or below the resolution limit of the optical microscope used in this analysis. The optical microscopic analysis of these high volume samples differs from the SEM analysis of the low volume samples in that detailed quantitative size distributions were not determined for these high-volume size distributions. In addition, the high volume samples do not have the sample collection efficiency problems of the low volume samples. Consequently, these optical microscopic analyses included many larger particles with $r > 10$ μm that the SEM analysis did not include.

The composition was somewhat variable, but the major components (by volume) appear to be the silicate minerals and calcite. Calcite ranged up to 30% by volume in some of these samples, while the component which we have identified as

a feldspar-quartz component varies between 5% and 50% of the observed sample volume. The "chert" component ranges between 0% and 60% by volume.

Hematite is present in many of the samples analyzed. Its form ranges from large to small crystals, some of which are present as a dusting on other grains. The amount of hematite present does not appear to be directly related to the measured absorption of these samples. The brownish aggregates consist of small quartz grains, clays, and ohter minerals, including limonite. The coloration is consistent with limonite as a component of the aggregates.

In these samples, as in all of the other samples which we have investigated, the absorbing material is present in aggregates with other particles or as smaller grains "dusting" or coating the larger grains. No separate population of small highly absorbing particles is seen.

These samples differ from the Saharan samples measured during the GATE program in two ways: There is more variation in physical and optical properties in these samples, and the overall sample size measured during MONEX was considerably larger than that measured during GATE.

These differences are due to the fact that the GATE samples were collected considerably further from the aerosol source regions allowing both greater mixing and removal of the larger particles by sedimentation. Since the larger particles viewed through the optical microscope show more variation in composition than the smaller particles with $r \sim 1$ μm, their removal will be expected to reduce the intrinsic sample variation. In addition, the Saharan aerosol, as measured during GATE, is probably from a somewhat restricted source region. These MONEX samples, by comparison, were collected in such a way that aerosols from several different source regions were samples. Samples were collected in or near source regions during our flights over India and Saudi Arabia (particles as large as 200 μm radius were seen). Our oceanic samples analyzed by optical microscopy were collected within a few hundred kilometers of the aerosol sources.

REAL COMPONENT OF REFRACTIVE INDICES

An average n_{RE} value (for white light illumination) was calculated for each of the samples analyzed by optical microscopy. This average n_{RE} was calculated by means of a volume weighted average of the n_{RE} values determined by the microscopic analysis. These average n_{RE} values are shown in Table V.

Although, as we have seen, there is a good deal of intrinsic variation in composition, the average values of n_{RE} calculated for these samples shows much less variation. These average values range between 1.58 and 1.66; the mean value of n_{RE} calculated for this set of samples is 1.61. This overall average value of n_{RE} is somewhat larger than other measurements, such as those of the Saharan aerosols, possibly due to a greater relative importance of higher index materials such as the colored grains and the hematite. The differences, however, should have only minor significance for radiative calculations.

ABSORPTION MEASUREMENTS

As discussed above, the samples for which the aerosol absorption was measured were collected within the haze layer and also at high altitudes of ≈ 11-13 km, well above the bulk of the haze layer, which extended to an altitude of ≈ 5 km.

These absorption data are shown in Figs. 8, 9, 10, 11, 13, 14, and 16. The absorption data for each of the samples are also given in tabular form in Appendix A. The data have been grouped into measurements made over Saudi Arabia, including measurements on adjacent oceanic regions made on the Dhahran flights; measurements made above and within the haze layers made above the Arabian Sea; measurements made over India; and high altitude measurements made outside the MONEX study area.

Saudi Arabian Measurements

The general area in which each of the samples was collected has been shown in Fig. 7. Representative flight tracks are shown in the figure for regional energy budget missions (A) and differential heating missions (B). Fig. 7 and the following maps have been adapted from Smith et al. (1980). Wavelength dependent n_{IM} data for these samples are shown in Fig. 8 (within haze data) and Fig. 9 (above haze data). The within-data on Fig. 8 includes M4, DF-I, DF-II, and M6, M7, M8, and M10.

The M4 data were primarily collected within the haze layer near Dhahran, although the sample includes some high altitude aerosol. The DF-I and DF-II samples were collected as dustfall samples during a haboob episode at Dhahran. The other four samples were collected during low level flights over Rub'al Khali,

the area that is the center of the heat low over Saudi Arabia (see Fig. 7). These four Rub'al Khali samples show very consistent values of absorption even though the samples were collected on four different sampling days, suggesting that they may represent some average value of aerosol absorption for the region.

The differences that are seen in this data set and the other within-haze layer data sets may be associated with different source regions for the aerosols. Meteorological analysis of Krishnamurty et al. (1982) was used to infer possible different source regions for these aerosols. The analysis for 850 mb, which we have assumed to be most representative of the altitude at which the low level dust transport across Arabia occurs, indicates that the most likely sources for our measured, low level aerosols are the desert regions of southern Saudi Arabia, that is the aerosols are relatively local. Both DF-I, DF-II, and M4 by contrast appear to be from northern and central reigons of Arabia, with the two dustfall samples having an important local Dhahran component. For calculations of regional heating effects, we recommend that the average of the four low level Rub'al Khali samples be used.

The high altitude Saudi Arabian samples are shown in Fig. 9. The M9 and M11 samples have absorption characteristics quite similar to our low level Rub' al Khali samples. Based on the Krishnamurty meteorological analysis, the source for these aerosols appears to be the desert areas of Saudi Arabia or Northwestern Africa. Because of the similarity with the Rub'al Khali samples we infer that these represent Saudi desert samples that have been lifted to these altitudes by convective activity. The M3 sample exhibited somewhat higher absorption; its concentration was low, and its source was ill defined; possible sources range from the area of the Horn of Africa to northern Arabia. It was collected on the same flight as within haze sample M-4 and appears to have quite similar absorption

characteristics as M-4. M5 has absorption significantly higher than the other samples. The wind trajectories suggest a source in the Mediterranean region.

Arabian Sea Samples

The absorption values measured for our Arabian Sea samples are shown in Fig. 10 (within-haze data) and Fig. 11 (above haze data). The within-haze data set consists of samples ME1, M14, M27, M28, M31, and M32. Absorption values at 500 nm shown on this figure range from ≈ .002 to ≈ .01 for sample M14. Sample ME1, unlike the other aircraft samples discussed here was collected on the NCAR Electra aircraft using the standard Electra sampling system rather than the NASA CV-990. The samples ME1 and M14 have the highest absorption of the samples shown in this figure. The location of the flights in which these samples were collected are shown in Fig. 12. Wind trajectory analysis for 700 mb and 850 mb suggest that these aerosols are transported from northern India and Iran.

The other samples shown in Fig. 10 were collected during flights on June 22 (M27 and M28) and June 26 (M31 and M32). The locations of these flights are shown in Fig. 12; each of these four samples was collected near 17°N, 65 E. M27 was collected at an altitude of ≈ 12,000 ft; 700 mb wind trajectories indicate air flow from the Rub al Khali desert. Sample M28 was collected between 8,000 and 1,000 ft; 850 mb trajectories suggest Saudi Arabia or the Horn of Africa as the aerosol source. M31 was collected between 15,000 and 5,000 ft; M32 was a low level sample collected at an altitude of 2,000 ft. Trajectories suggest eastern Saudi Arabia or western Iran as the source. Sample M31 which has the lowest absorption appears to be from approximately the same location as aerosols investigated by Otterman et al. (1981) by means of satellite imagery. The absorption measured for this sample is approximately the same as that inferred by Otterman et al for their samples.

Representative flight tracks during which the above haze Arabian Sea samples were collected are also shown in Fig. 12. There is somewhat less variation in absorption properties for these samples than for some of the other data sets. Wind trajectories at the 200 mb level would suggest southern Indian sources for most of these samples. On these flights, however, there was generally evidence of convective activity (except for the M13 sample) which would result in mixing of some aerosols from the main haze layers below 5 km up to the flight altitude of 11-13 km. Because of this mixing, the sources for these aerosols are considered to be indeterminant.

Indian Samples

The absorption values measured for the samples collected over India are shown in Figs. 13 (within-haze) and 14 (above-haze). The flight tracks for the two data flights over India are shown in Fig. 10. Samples M17 and M18 were from the flight leg A in Fig. 15 between New Delhi and Calcutta. Sample M17 was collected at altitudes between 6.1 and 3.4 km; sample M18 was collected at $\sim$ 0.3 km altitude. The two samples represent separate and distinct haze layers, and the optical properties of the aerosols in each of these haze layers are distinct. The lower aerosol haze particles have lower absorption by a factor of $\sim$ 3 than those in the upper layer. Samples M20 and M21 were collected from the approximate positions B(M20) and C(M21). Samples were collected between 4 and 2 km (M20) and between 3 and 1 1 km (M21). Winds in each case were from the west to west-northwest; but on those flight days as on nearly all of the pre-onset days these were high dust loadings over north central and north-western India. We have not attempted to estimate any specific sources for these haze layers.

Outside of MONEX Study Area

Absorption values for a set of four samples collected on ferry flights to and from the MONEX study area are shown in Fig. 16. M1 was collected over land areas of North America and over the Atlantic Ocean on the flight series between San Francisco and Geneva. M2 was collected over international waters of the Mediterranean. Samples M35 and M37 were collected over international waters between Bangkok and Hong Kong (M35) and between Tokyo and Anchorage (M37). These samples fall neatly into two categories: those with relatively high absorption collected over North America, the Atlantic and the Mediterranean, and those with relatively low absroption collected over southeast Asia and the Pacific. The two high absorption samples show the influence of some non soil absorber.

The surprising aspect of these samples is the high absorption measured at these these high altitudes, even in regions considerably removed from major dust injection into the upper troposphere.

OVERVIEW OF MONEX AEROSOL RESULTS AND RELATION TO RADIATION MEASUREMENTS

Aerosol Measurements

These measurements provided data on sizes, concentrations, and the physical and optical properties of aerosols in the MONEX study area. Size distributions determined by SEM analysis of Nuclepore Filters show the dominance of soil-derived particles. Although our CV-990 low volume collection apparatus has reduced collection efficiency for particles larger than 1 μm radius, our size distribution analysis indicates that the aerosols over India, Saudi Arabia, and adjacent oceanic regions have sizes that are quite similar to those measured previously for such soil derived particles. There were indications, as well, of the presence of particles smaller than the soil particles that would have little or no effect on total mass, but could have some minor effect on the radiative properties. Optical microscopic analysis of selected high-volume filters showed a greater variation in composition than seen in our earlier Saharan measurements due to the larger number of sources for these MONEX aerosols and the greater proximity to these sources. No separate population of highly absorbing small particles was seen.

Optical properties measured for these aerosols showed n_{RE} (real component of refractive index) values near 1.6 for this data set. n_{IM} (imaginary component of refractive index - an absorption parameter) values showed more variation. All of the values measured within the haze layers were in the range expected for soil derived aerosols. Measurements over Saudi Arabia showed values near .004 between 500 and 700 nm, with slightly higher values measured at shorter wavelengths. Other measurements within the haze layer show the same qualitative character, with

500 nm values ranging between $\sim$ .014 and .002. Measurements above the main haze layers show more variation in measured absorption; in some cases, surprisingly high values of n_{IM} were measured. We were able, in some cases, to relate our aerosol samples to specific source regions.

Concentration Measurements and Mass-Visibility Relations

The goal of a comprehensive radiation experiment as discussed by Kondratyev (1973) requires the calculation of radiative parameters for comparison with the directly measured ones. We have made these calculations, and in this and the following sections, we will discuss these results in relation to radiative measurements reported by Ackerman and Cox (hereafter referred to as AC), as well as in relation to other concurrent observations made during the flights. Since the radiation measurements are parameterized according to mass loading and our calculations are parameterized according to optical depth and aerosol optical properties, some discussion of the relationships between the different data sets is necessary.

Our first such comparison is between the concentrations inferred from the optical particle counters and our filter measurements. Some equivalent data from the lowest flight levels over the Rub'al Khali desert are shown in Table VI. The AC data are taken from their paper. Our data are adapted from Table I with some correction to account for the time spent at altitudes above the 0.3 km altitude. The AC data indicate higher aerosol concentrations than do ours. Since both sets have potential uncertainties (the optical particle counter with particle size calibration and response uncertainties and our sampling system with sampling efficiency and detailed flow calibration uncertainties) we have checked the consis-

tency of the two data sets with other observations using mass-visibility relations such as those discussed by Pilat and Ensor (1971) and by Patterson and Gillette (1977). We have used both simultaneous visibility observations from the aircraft as well as numerical calculations of optical quantities from log-normal approximations to the AC and to our size distributions.

Patterson and Gillette tabulated various values of the parameter C defined by the equation

$$C = MV$$

where C is the mass concentration measured in g m^{-3} and V is the visibility measured in km. Values of C were calculated for the low-level Saudi MONEX data sets. Visibilities were estimated by observers aboard the NASA CV-990, and C values were calculated using both the AC data and our mass concentration data. The values are shown in Table VI. The data of Patterson and Gillette showed that for particles with $r < 20$ μm the average value of C was 1.7×10^{-2} g m^{-3} km. The AC data show C values larger than this avearge, our data values somewhat smaller.

Calculations of mass concentration-extinction (M/σ_E) ratios as shown in Table VII gives similar results. The Patterson and Gillette C implies an M/σ_E ratio of ~ 4. The AC ratios are larger than this average value; our data, the PGP data, generally show values that are smaller than this average.

We have approximated the fitted AC distribution for Flight 8 with a log-normal distribution with a mean radius of 2.6 μm and a standard deviation (σ) of 1.75. For this distribution our calculations indicate an M/σ_E ratio of 9.3 (assumed $\rho = 2.5$ g/cm^3) so that their measured distributions are in general consistent with observed extinctions. An M/σ_E ratio of 2.7 was calculated on the

basis of the mode parameters (mean radius and standard deviation) inferred for our SEM determined soil particle mode. If we arbitrarily double the inferred mean radius from 0.4 μm to 0.8 μm, as a very approximate way of accounting for the effects of particle sampling losses, the M/σ_E value calculated is 5.8.

Inclusions of the effects of the small particle mode near 0.2 μm radius will cause some lowering of the inferred M/σ_E values since M/σ_E for this small particle mode is only 0.23 g/m^2 (assuming $\rho = 2$ rather than the 2.5 value appropriate for the soil particles).

We may expect the actual M/σ_E value to be between 2 and 9, with somewhat lower values possible under conditions of low soil aerosol concentrations. Since all of the data are approximately in this range, these mass-visibility or mass-extinction relations do not allow us to choose one of the concentration data sets over the other. There do appear to be considerably more small particles present than measured by AC on at least one of the flight days. These added small particles present would cause an increase in the total mass and a decrease in the inferred values of the mass concentration visibility constant. On the basis of all of the data we estimate that the volume mean radius (r_v) will be between that inferred for our SEM data (r_v = 2 μm) and that inferred from the AC data (r_v = 7 μm).

Optical Depth Inferences

The total optical depth τ, defined according to the equation $\tau = \ell n(I/I_o)$, was not measured directly during these Arabian desert flights. We have inferred optical depths for the 4 low level Arabian flights by two methods. τ_{ML} was determined from the column mass loadings presented by AC using the mass- extinction ratio appropriate for their distributions. This simple procedure was used because

of the relative uniformity of the size distributions measured by AC. An alternate optical thickness estimate τ_{SC}, was determined from visual range observations from the aircraft at high altitudes. Given the estimates of this slant visual range, a path length V' in the dust layer was calculated and an average extinction $\bar{\sigma}_E$ was calculated from the equation

$$\bar{\sigma}_E = \frac{2.1}{V'}$$

This relation differs from the more familiar Koschmeider relation $\sigma_E = 3.9/V$ for three reasons: the observed contrast is between objects of similar relative brightness rather than dark objects against the horizon; the aerosols are absorbing (see Roessler and Faxvog, 1981) and the objects have smaller angular dimensions than those prescribed the usual Koschmeider relation (Gordon, 1977; 1980).

Mid-visible optical depths inferred by these methods are shown as τ_{ML} and τ_{SD} in Table VIII. These τ_{ML} estimates are generally lower than the τ_{SD} estimates, but the values agree to within a factor of 2. The closest agreement is seen in Flight 9 where the two estimates of τ differ by only 40%. It appears that the average optical depth on these flights is between 0.5 and 1.

Calculations of Radiative Properties and Comparison with Measured Values

AC measured quite uniform size distributions for the four low level flight patterns over the Rub'al Khali; our meausred absorption properries were also quite uniform for these four samples. Taken together, these data indicate a good deal of uniformity in the aerosol for these four days, so that a representative set of the measured optical constants should be valid for each of the four sampling flights.

We have used Mie theory to calculate the scattering, absorption and extinction properties of the aerosol. Our measured optical constants were used, and calculations were made for several different log-normal size distributions as a check on the importance of the differences in these measured size distributions. A representative set of results of these calculations for phase function, extinction and scattering for a nominal concentration of 1 particle/cm^3 and the appropriate log-normal size distribution parameter for λ = .55 μm is shown in Fig. 17 (r_g = 2.6, σ = 1.75 - AC Distribution), Fig. 18 (r_g = .4, σ = 2.18 SEM Distribution), Fig. 19 r_g = .8, σ = 2.18 - Modified SEM Distribution), and Fig. 20 (r_g = .14, σ = 1.57 - SEM Small Particle Distribution).

The single scattering albedo, ω, which is the ratio of aerosol scattering to extinction, calculated for λ = 0.55 μm ranges from 0.88 for the SEM distribution to .73 for the AC distribution. Other calculations for wavelengths between 0.5 and 1 μm show that the total particle extinction is approximately constant with wavelength, with values increasing slightly with increasing wavelength between 0.5 and 1 μm. At 0.7 μm, ω ranges from 0.90 for the SEM distributions to 0.77 for the AC distribution. g was not calculated for these distributions but was assumed to be $\sim$ 0.75 on the basis of previous calculations.

We have used two sets of radiation measurements discussed by Ackerman and Cox for our aerosol comparison; a set of satellite spectral reflectance measurements in the 0.55 - .9 μm wavelength band over the Arabian deserts and a set of fractional absorptance date inferred from the TIROS-N satellite; these reflectance data were plotted by AC as a funciton of the column mass loading. A delta Eddington radiation transfer routine (Baker and Coletti, 1982) was used to calculate upward fluxes from an aerosol layer over a surface with an albedo of 0.41 for radiation incident with cosine of the zenith angle (μ_o) equal to 0.9. Our calculations were made for 3 different optical depths (1,2,4) and for 4 different values of ω (.99, .95, .90, .80).

Calculations were also made for μ_o values of 1.0 and .8; these showed no significant differences in upwelling flux. The results of these calculations are shown in Fig 21; the satellite reflectance data is also shown in this figure. For comparison with our calculations, the AC reflectance data has been presented as a function of optical depth, using mass-extinction relations discussed above to change from column mass loading to optical depth.

This figure indicates that the reflectance data is best matched with an ω slightly less than 0.9. Use of the other value of τ derived from our slant visual range estimations would have only a slight effect on the comparisons. the best match would still be an ω of $\simeq$ 0.9. Values of ω at 0.7 μm were used for the comparison. They suggest a distribution with a mean size intermediate between our SEM distribution and the measured AC distribution. The comparison also suggests that our measured absroption properties do reasonably represent the actual aerosol absorption properties.

Detailed calculations of bidirectional reflectance were not made, since the upwelling radiation emerging from the Rub'al Khali desert were measured to be nearly isotropic. Although our claculations must be considered as approximate, the overall trend of the data with increasing optical depth does indicate an appreciable absroption due to the desert aerosols.

We have also used our measured aerosol properties in our radiative transfer model to calculate average heating rates within the aerosol layer due to the absorption of short wave radiation. For these calculations we assumed an aerosol with an ω of .85, an optical depth of 0.8, and an incident cosine of 1.0. The calculated fractional absorptance is 0.20, which, for the 5 km layer, implies an average local noon heating rate of 0.2°C/hour throughout the haze layer due to the absorption of short wave radiation. This value is somewhat larger than the heating rates inferred by Ackerman and Cox.

A further comparison has been made with the fractional absorptance measured by AC. They used their measured radiative divergences to infer the fractional absorptance of solar energy in the haze layer as a function of the density weighed path length of the radiation in the layer. The density weighed path length is just the column mass loading of the aerosol above the haze layer times the secant of the solar zenith angle. The AC best fit inferred fractional absorptance is shown in our Figure 22.

We have calculated the fractional absorptance in the haze layer using the delta Eddington routine for parameters that are appropriate to the conditions of Flight 9, in which the low level flight leg was flown in the early morning. τ was assumed to be 1 on the basis of the mass-extinction relations discussed above and the calculations assumed an incident cosine of 0.1. Use of column mass loading values of Table VIII for this flight and an incident cosine of 0.1 gave an equivalent density weighed path length of 80 g/m^2 for our calculations.

The delta Eddington calculations were made for g = .75 and for ω values of .80, .90, .95, .96, and .97. These calculated fractional absorptances are also shown in Fig. 27. These calculations indicate that an ω of $\approx$ 0.96 is required to produce the fractional absorptance measured by AC. The ω values between 0.8 and .9 expected on the basis of the aerosol measurements and the satellite reflectance comparison would result in considerably more fractional absorptance than measured by AC. Although this comparison, like the others, is only approximate, it suggests that there may be a significant difference in the inferred short wave absorption from the two data sets. The reason for this difference is not known at this time.

To sum up these results, our comparisons show a general agreement between the reflectances calculated on the basis of our estimates of aerosol optical pro-

perties and satellite measurements. Both the measurements and the calculations indicate significant short wave heating. Calculations of short wave absorption and heating within the layer, however, using our measured optical properties, imply a larger absorptance and a larger average short wave heating than inferred from the flux divergence measurements. These differences appear to be larger than those expected on the basis of measurement uncertainties.

REFERENCES

Ackerman, S.A. and S.K. Cox, 1982: The Saudi Arabian Heat Low: Aerosol distributions and Thermodynamic Structure. J. Geophys. Res., 87, 8991-9002.

Baker, M.B. and A. Coletti, 1983: Uncertainties in the evaluation of the shortwave radiative properties of an aerosol layer due to experimental and numerical errors. Appl. Opt., 21, 2244-2252.

Gordon, J.I., 1980: Daytime Visibility, A Conceptual Review, University of California, San Diego, Scripps Institution of Oceanography, Visibility Laboratory, SIO Ref. 80-1.

ICSU/WMO, 1976: The Monsoon Experiment. GARP Publications Series #18, World Meteorological Organization, Int. Counc. Sci. Unions, Geneva, Switzerland.

Kondratyev, K. Ya., 1973: The complete atmospheric energetics experiment. GARP Publ. Ser., 12, 43 pp., World Meteorol. Organ./Int. Counc. of Sci. Unions, Geneva.

Krishnamurty, T.N., P. Grieman, Y. Ramanthan, R. Pasch, P. Ardanuy, 1980: Quick Look Summer MONEX Atlaa Part I and Part II, FSU Report 80-4, The Florida State University, Tallahassee, Florida 32306.

Otterman, J., R.S. Fraser and O.P. Baheti, 1982: Characterization of tropospheric desert aerosols at solar wavelengths by multispectral radiometry from landsat. J. Geophys. Res., 87, 1270-1278.

Patterson, E.M., 1981: Optical properties of the crustal aerosol: Relation to chemical and physical characteristics. J. Geophys. Res., 86, 3236-3246.

Patterson, E.M. and B.T. Marshall, 1982: Diffuse reflectance and diffuse transmission measurements of aerosol absorption at the First International Workshop on Light Absorption by Aerosols. Appl. Opt., 21, 387-393.

Patterson, E.M. and D.A. Gillette, 1977: Measurements of visibility vs mass concentration for airborne soil aprticles. Atm. Environ., 11, 193-196.

Patterson, E.M., C.S. Kiang, A.C. Delany, A.F. Wartburg, A.C.D. Leslie, and B.J. Huebert, 1980: Global measurements of aerosols in remote continental and marine regions. Concentrations, size distributions, optical properties. J. Geophys. Res., 85, 7361-7376.

Patterson, E.M. D.A. Gillette and B.H. Stockton, 1977: Complex index of refraction between 300 and 700 nm for Saharan aerosols. J. Geophys. Res., 85, 3153-3161.

Peterson, J.T., 1968: Measurements of atmospheric aerosols and infrared radiation over northwest India and their relationship. Ph.D. thesis, University of Wisconsin.

Pilat, M.J. and D.S. Ensor, 1971: Comparison between the light extinction aerosol mass concentration relationship of atmospheric and air pollutant emission aerosols. Atm. Environ., 5, 209-215.

Roessler, D.M. and F.R. Faxvog, 1981: Visibility in absorbing aerosols, Atm. Environ., 15, 151-555.

REFERENCES

Smith, E.A., S.A. Ackerman, S.K. Cox, T.H. Vonder Haar, 1980: Summer MONEX High Altitude Aircraft Radiation Measurements, Technical Report, Colorado State University, Fort Collins, Colorado.

Table I.

MONEX Aerosol Concentrations - Within Haze Layer

Sample ID	Dates	Location*	Approximate Altitude (km)	Ambient Concentration ($\mu g/m^3$)	Mixing Ratios (PPBM)
DF1		SA	surface		
DFII		SA			
M4**	5-6,5-9,5-12	SA	variable	--	
M6	5-9	SA	<1	1100	1000
M7	5-10	SA	<1	380	320
M8	5-12	SA	<1	590	490
M10	5-14	SA	<1	200	170
M12**		AS	variable	--	--
M14	5-31	AS	variable (1-8km)	--	24
ME1	6-4	AS	variable (6 km)	--	80
M17	6-5	I	5	80	100
M18	6-5	I	<1	85	71
M20	6-11	I	3	110	125
MM21	6-11	I	3	550	620
M27	6-22	SAS	4	160	190
M28	6-22	SAS	variable (<1-3)	--	420
M31	6-26	AS	2	3300	3200
M32	6-26	AS	<1	460	380

*SA - Saudi Arabia, AS - Arabian Sea, I - India

Table II.

MONEX Aerosol Concentrations - High Altitude

Sample ID	Dates	Location*	Approximate Altitude (km)	Ambient Concentration ($\mu g/m^3$)	Mixing Ratios (PPBM)
M1		F1	10	1.1	2.5
M2		F2	10	2.4	5.4
M3	5-6	SA	9	1.4	3.0
M5	5-7;5-10	SA	11	13	32
M9	5-14	SA	10	9.8	22
M11	5-18	SA/AS	11	110	282
M13	5-31	AS	10	.64	1.5
M15	6-03;6-07	AS	11	.50	1.2
M16	6-05	I	10	21	48
M19	6-11	I	10	1.4	3.2
M22	6-12	AS	11	18	43
M23	6-14	AS	9	3.9	8.1
M24	6-15	AS	10	2.1	4.6
M25	6-17;6-18	AS	11	3.2	7.8
M26	6-22	AS	10	1.5	3.4
M33		F3	11	<0.2	<0.5
M35		F4	11	1.6	3.9
M36		F5	11	<1.0	<4
M37		F6	11	1.0	2.5

SA - Saudi Arabia, AS - Arabian Sea, I - India, F - Ferry flights outside of MONEX study area.

Table III.

Geometric Mean Mass Mixing Ratios for MONEX Aerosols

Within Haze Layer

Saudi Arabia	280 ppbm
Arabian Sea	240 ppbm
India	150 ppbm

Above Haze Layer

Saudi Arabia	28 ppbm
Arabian Sea	50 ppbm
India	12 ppbm

Table IVa.

MINERALOGY, COMPOSITION, AND REFRACTIVE INDEX FOR SELECTED MONEX SAMPLES

Sample Location	M-6[a] SA		M-8[b] SA		M-11[c] SA/AS		M-12[d] AS	
Mineral Component (n_{RE})	% by volume	grain size	% by volume	grain size	% by volume	grain size	% by volume	grain size
Calcite (1.49-1.67)	35	2-35	20	2-25	--		20	1-15
Feldspar/Quartz (1.56)	8	2-15	50	2-60	15	4-15	20	1-9
Chert (1.56)	--		--		60	4-150	--	--
Brownish Aggregates (1.56)	50	4-35	25	2-45	10	9-125	35	5-110
Colored grains[+] (1.7)	--		3	9-60	10	4-25	5	5-9
Opaques	7	1.15	2	4-25	Trace	---	20	4-40

[+]Mostly biotite, horneblende, and some epidote

[a]Hematite present as dusting on grains; opaques contain hematite

[b]Trace of Hematite in the 1-10 μm range

[c]Virtually no hematite

[d]Trace of fine hematite and other opaques 0.3 to 3 μm

Table IVb.

MINERALOGY, COMPOSITION, AND REFRACTIVE INDEX FOR SELECTED MONEX SAMPLES

Sample Location	ME-1[e] AS		M21[f] I		M28[g] AS		M31[h] AS	
Mineral Component (n_{RE})	% by volume	grain size	% by volume	grain size	% by volume	grain size	% by volume	grain size
Calcite (1.49-1.67)	10	4-9	25	2-8	40	1-15	30	2-18
Feldspar/Quartz (1.56)	5	4-15	45	2-18	40	1-6	30	2-15
Chert (1.56)	35	2-30	--		--		--	
Brownish Aggregates (1.56)	35	9-90	10	1-450	15	5-45	35	4-30
Colored grains[+] (1.7)	--		--		--		--	
Opaques	10	3-70	10	4-18	--		<5	1-80

[+]Mostly biotite, horneblende, and some epidote

[e]Hematite present as dusting on grains; opaques contain hematite

[f]Trace of Hematite in the 1-10 μm range

[g]Virtually no hematite

[h]Trace of fine hematite and other opaques 0.3 to 3 μm

Table V.

Overall Estimate of Mid-Visible n_{RE}

Sample	n_{RE}
M6	1.60
M8	1.58
M11	1.60
M12	1.66
ME1	1.63
M21	1.65
M28	1.59
M31	1.59

Table VI.

Observed Mass Concentration-Visibility Relationships
for Low Alttitude Flight Legs

Flight	Observed V (km)	Mass Concentration AC ($g\ m^{-3}$)	MV - (AC) ($g\ m^{-3} km$)	Mass Concentration (PGP) ($g\ m^{-3}$)	MV - (PGP) ($g\ m^{-3}\ km$)
7	8	3.3×10^{-3}	2.6×10^{-2}	2.1×10^{-3}	1.7×10^{-2}
8	11	3.2×10^{-3}	3.5×10^{-2}	$.53 \times 10^{-3}$	5.8×10^{-3}
9	10	3.3×10^{-3}	3.3×10^{-2}	$.75 \times 10^{-3}$	7.5×10^{-3}
10	11	1.8×10^{-3}	2.0×10^{-2}	$.3 \times 10^{-3}$	3.0×10^{-3}

Table VII.

Mass-Extinction Relationships for Low Altitude Saudi MONEX Data

Flight	V	Total σ_E	Particulate σ_E	M/σ_E (AC)	M/σ_E (PGP)
7	8	$4.9 \times 10^{-4} m^{-1}$	$4.8 \times 10^{-4} m^{-1}$	6.9	4.4
8	11	$3.5 \times 10^{-4} m^{-1}$	$3.4 \times 10^{-4} m^{-1}$	9.4	1.6
9	10	$3.9 \times 10^{-4} m^{-1}$	$3.8 \times 10^{-4} m^{-1}$	8.7	2.0
10	11	$3.5 \times 10^{-4} m^{-1}$	$3.4 \times 10^{-4} m^{-1}$	5.3	0.9

Table VIII.

Estimates of Haze Optical Depth (τ) at Mid Visible Wavelengths

Flight	Column Mass Loading (g/m^2)	τ_{ML}	High Altitude Sight Distances (km)	τ_{SD}
7	4.1	.51	21	.96
8	4.9	.61	--	---
9	8.2	1.0	13	1.4
10	2.3	.29	37	.59

FIGURE CAPTIONS

Figure 1. The region in which the Arabian Sea portion of Summer MONEX occured (adapted from Smith et al., 1980).

Figure 2. SEM photographs of aerosols collected over Saudi Arabia during the low level portion of Flight 8. Fig. 2a shows the typical soil particle distribution; Fig. 2b shows the amorphous smaller particles.

Figure 3. A dN/d log r plot of the within-haze size distribution measured on Flight 8. The larger particle mode consists of soil derived particles, the smaller particle mode of the amorphous particle shown in 2b. The circles are measured data; the line is an approximate line presented to enhance the visualization of the mode structure rather than a best fit line.

Figure 4. A dN/d log r plot of the size distribution given by the solid line in Fig. 3 (+-+-+) with the simultaneous volume distribution measured by Ackerman and Cox (——).

Figure 5. SEM photographs of aerosols collected over India on Flight 17. The aerosol population appears to consist entirely of soil-derived aerosol.

Figure 6. dV/d log r distributions measured within the haze layer (o—o) and above the major portion of the haze layer (——) aboard the NCAR Electra aircraft over the Arabian Sea on June 4, 1979.

Figure 7. Representative flight tracks for regional energy budget missions (A) and differential heating missions (B). (Adapted from Smith et al., 1980).

Figure 8. Measurements of n_{IM} between 300 and 700 nm for samples collected within the haze layer over Saudi Arabia. The samples include DFI (o-o-o), DF-II (——), M6 (+-+-+), M7 (x-x-x), M10 (◊-◊-◊), and M4 (Δ-Δ-Δ). M4 includes some sample collected at high altitude.

Figure 9. Measurements of n_{IM} between 300 and 700 nm for samples collected above the haze layer over Saudi Arabia. The samples include M3 (——), M5 (o-o-o), M9 (Δ-Δ-Δ), and M11 (+-+-+).

Figure 10. Measurements of n_{IM} between 300 and 700 nm for samples collected within the haze layer over the Arabian Sea. The samples include M14 (——), ME1 (o-o-o), M27 (◁-◁-◁), M28 (+-+), M31 (x-x), and M32 (◇-◇).

Figure 11. Measurements of n_{IM} between 300 and 700 nm for samples collected above the haze layer over the Arabian Sea. The samples include M13 (——), M15 (o—o), M22 (Δ—Δ), M23 (+—+), M24 (x—x), M25 (◇—◇), and M26 (◁—◁).

FIGURE CAPTIONS

Figure 12. Representative flight tracks of the CV-990 over the Arabian Sea.

Figure 13. Measurements of n_{IM} between 300 and 700 nm for samples collected within the haze layer over India. The samples inlcude M17 (——), M18 (o-o-o), M20 (Δ-Δ-Δ), and M21 (+ ━ +).

Figure 14. Measurements of n_{IM} between 300 and 700 nm for samples collected above the haze layer over India. The samples include M16 (——), and M19 (o-o-o).

Figure 15. Flight tracks of the CV-990 on missions over India.

Figure 16. Measurements of n_{IM} between 300 and 700 nm for samples collected at high altitudes on ferry flights outside of the MONEX study area. The samples include M1 (□-□-□), M2 (o-o-o), M35 (Δ—Δ), and M37 (+-+-+).

Figure 17. Calculated optical properties for our log-normal approximation to the Ackerman and Cox aerosol size distribution. The calculations are made for a nominal concentration of 1 particle/cm^3 rather than the actual concentration.

Figure 18. Calculated optical properties for a log-normal approximation to our measured SEM soil-derived aerosol size distribution. The calculations are made for a nominal concentration of 1 particle/cm^3.

Figure 19. Same as Fig. 18, except that the calculations are made for a modified size distribution in which r_g is increased from 0.4 μm to 0.8 μm.

Figure 20. Same as Fig. 18, except that the calculations are made for the small particle size distribution in our SEM size distribution.

Figure 21. A comparison of the spectral reflectance measured in the 0.55-0.9 μm wavelength band by the TIROS-N satellite and reflectances calculated for an aerosol layer with ω = 0.8, .9, .95, and .99.

Figure 22. A comparison of fractional absorptance measured by Ackerman and Cox with that calculated by us for ω = .8 (o), .9 (Δ), .95 (+), .96 (x), and .97 (C). See text for details.

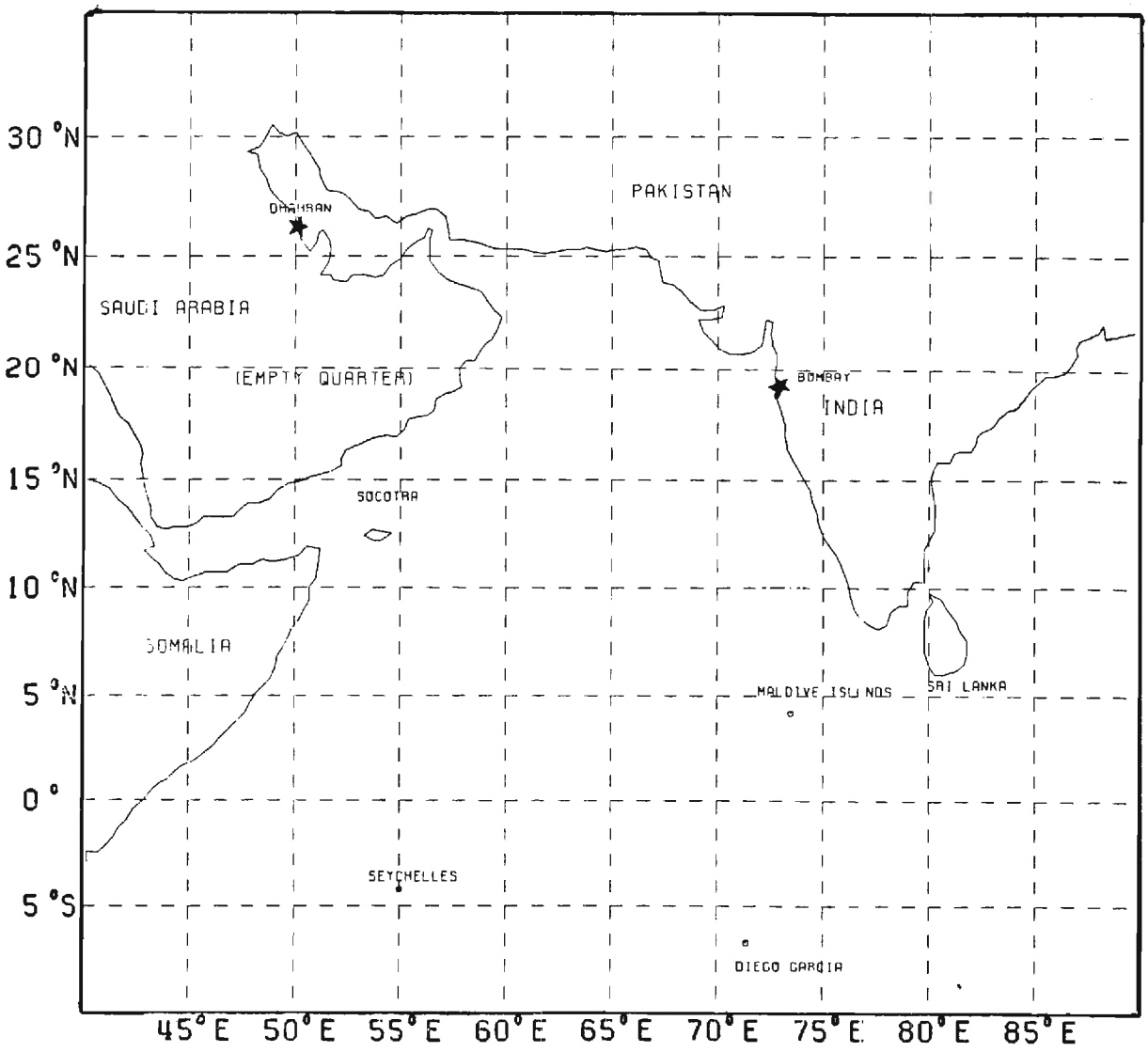
30 °N
25 °N
20 °N
15 °N
10 °N
5 °N
0 °
5 °S
45° E
50° E
55° E
60° E
65° E
70° E
75° E
80° E
85° E
PAKISTAN
DHAHRAN
SAUDI ARABIA
(EMPTY QUARTER)
BOMBAY
INDIA
SOCOTRA
SOMALIA
MALDIVE ISLANDS
SRI LANKA
SEYCHELLES
DIEGO GARCIA

Fig. 1.

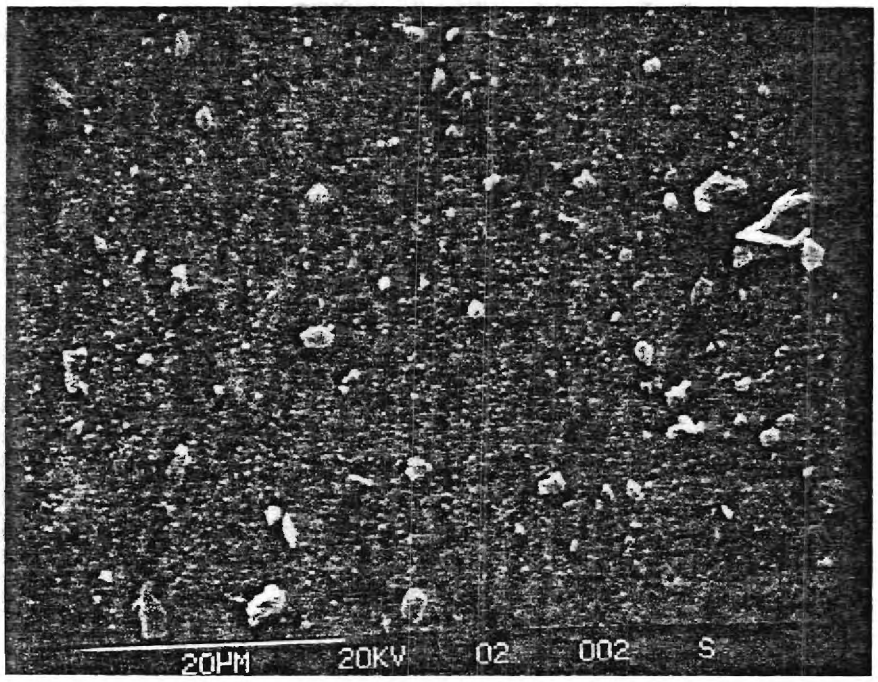

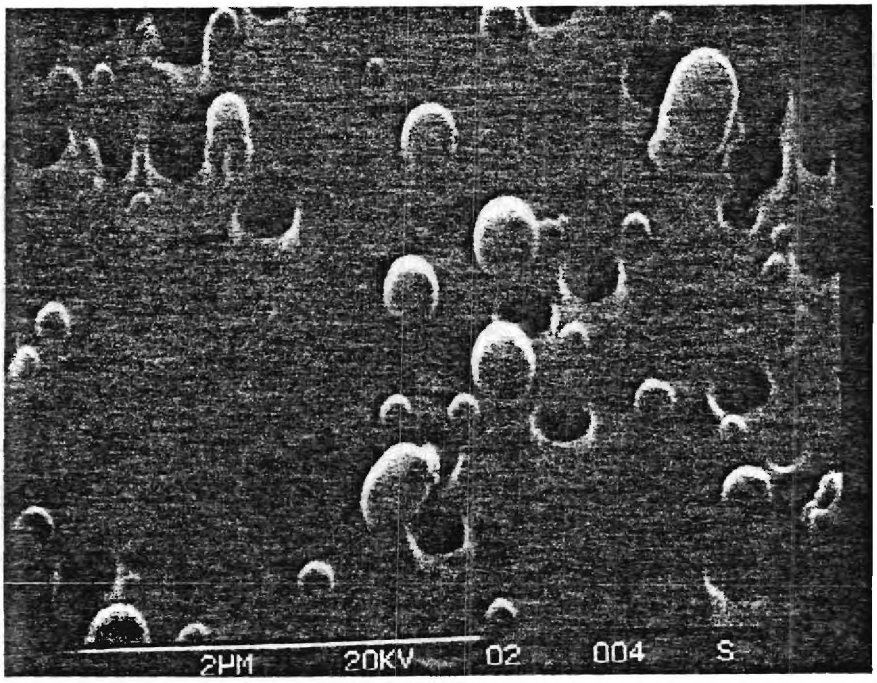

Fig. 2.

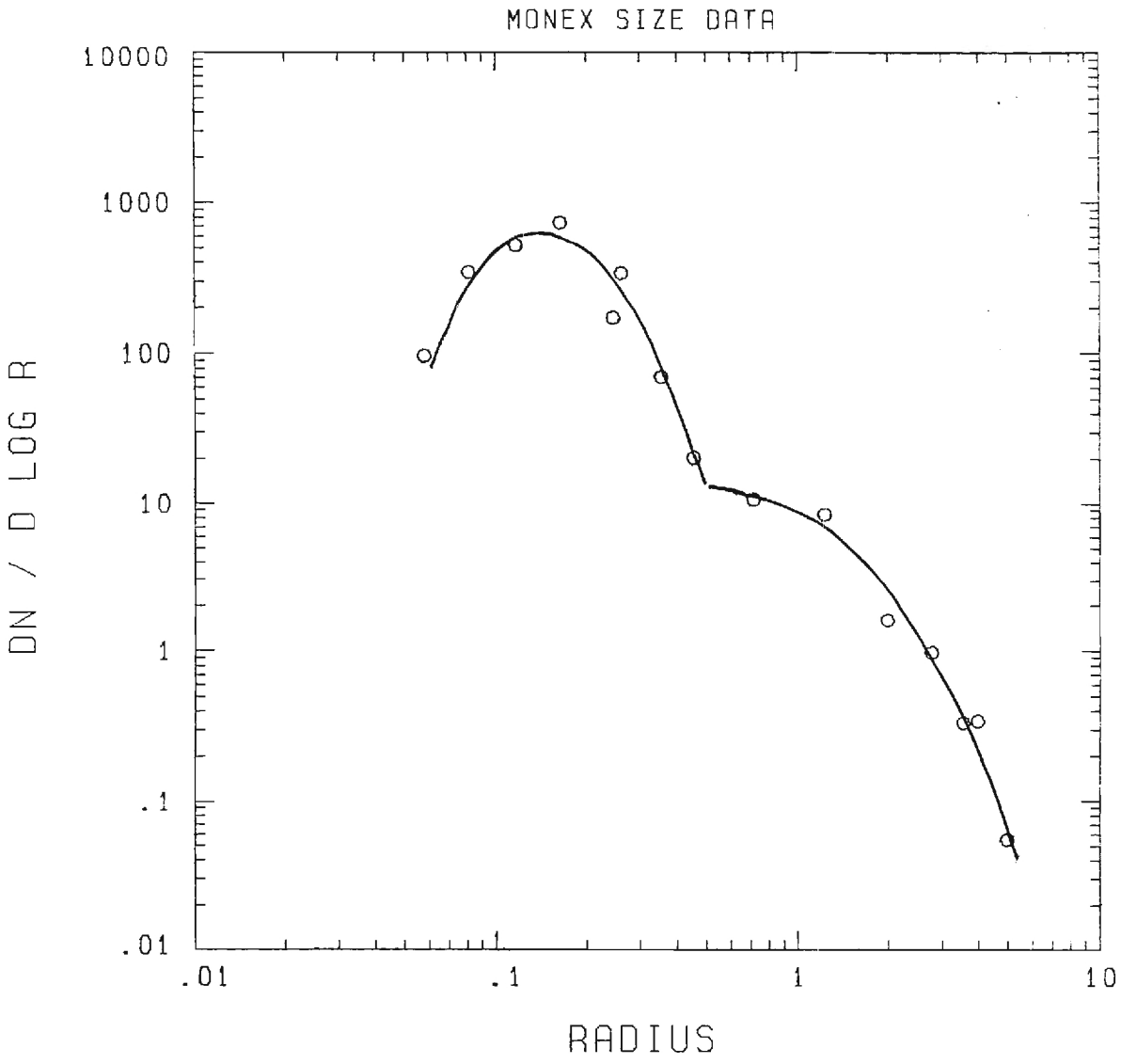
MONEX SIZE DATA
10000
1000
100
10
1
.1
.01
DN / D LOG R
.01
.1
1
10
RADIUS

Fig. 3.

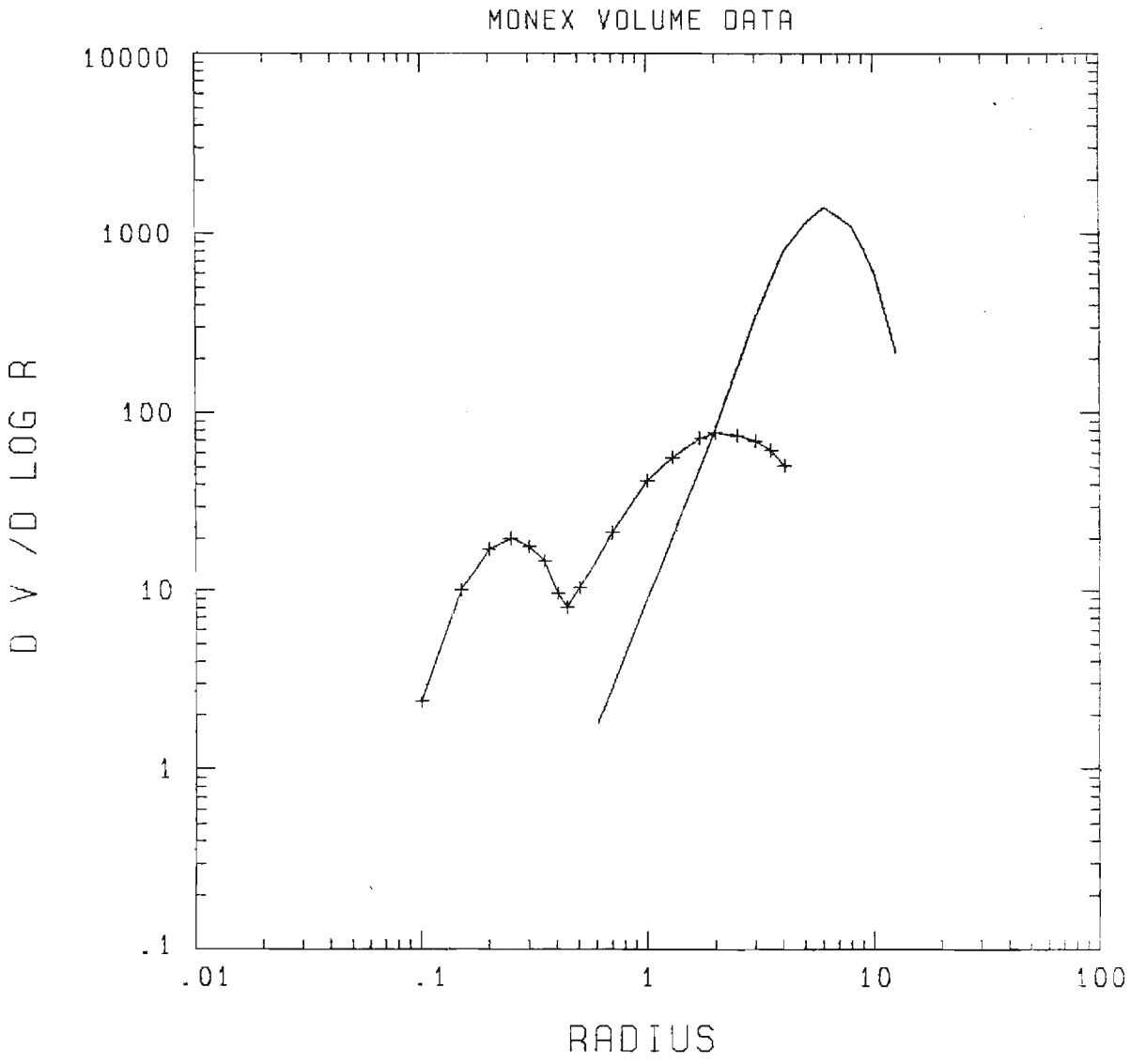
MONEX VOLUME DATA
10000
1000
100
10
1
.1
D V /D LOG R
.01
.1
1
10
100
RADIUS

Fig. 4.

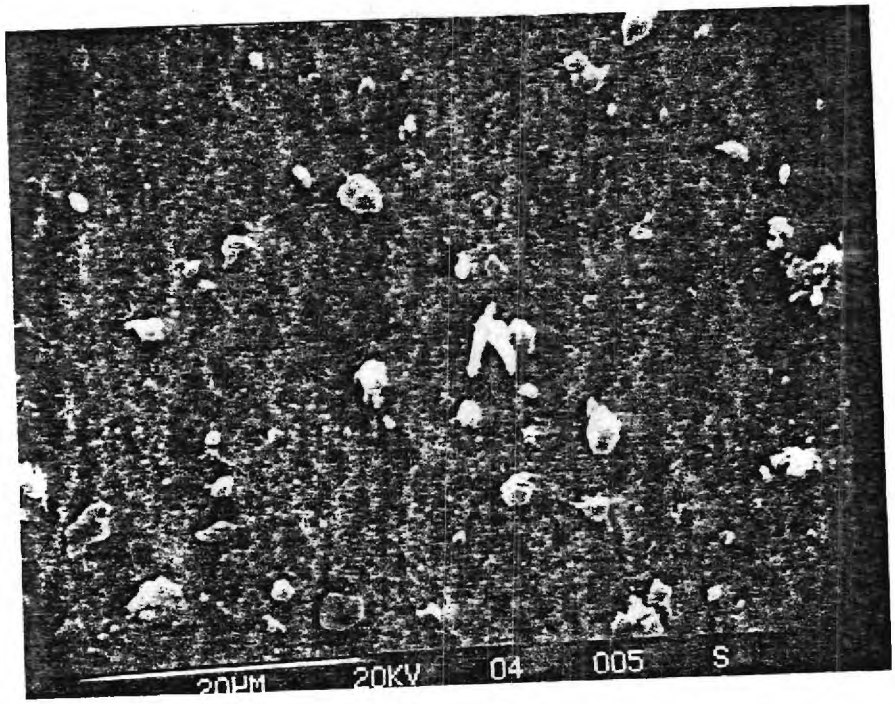

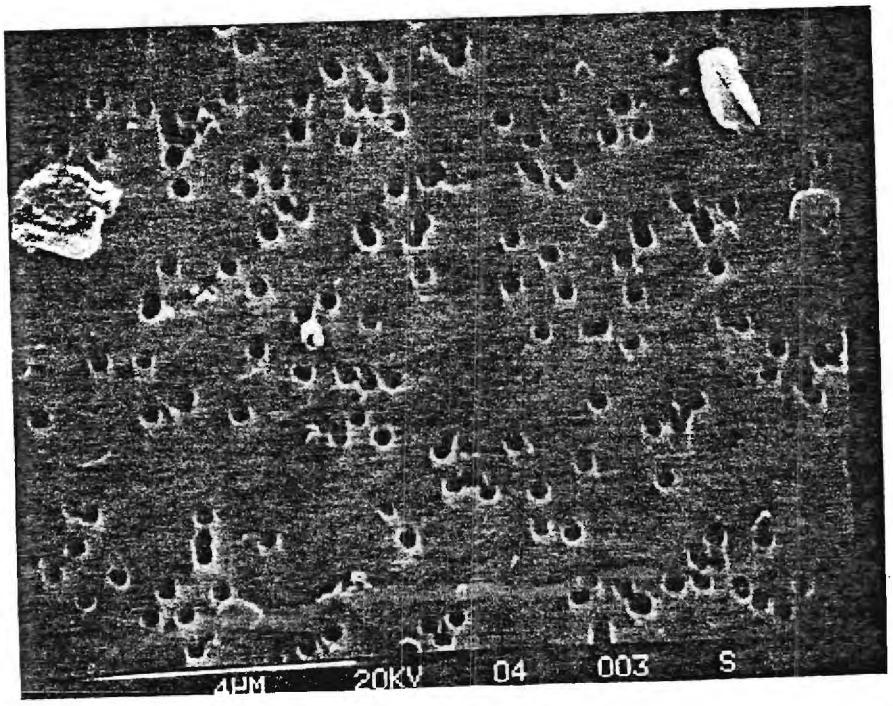

Fig. 5.

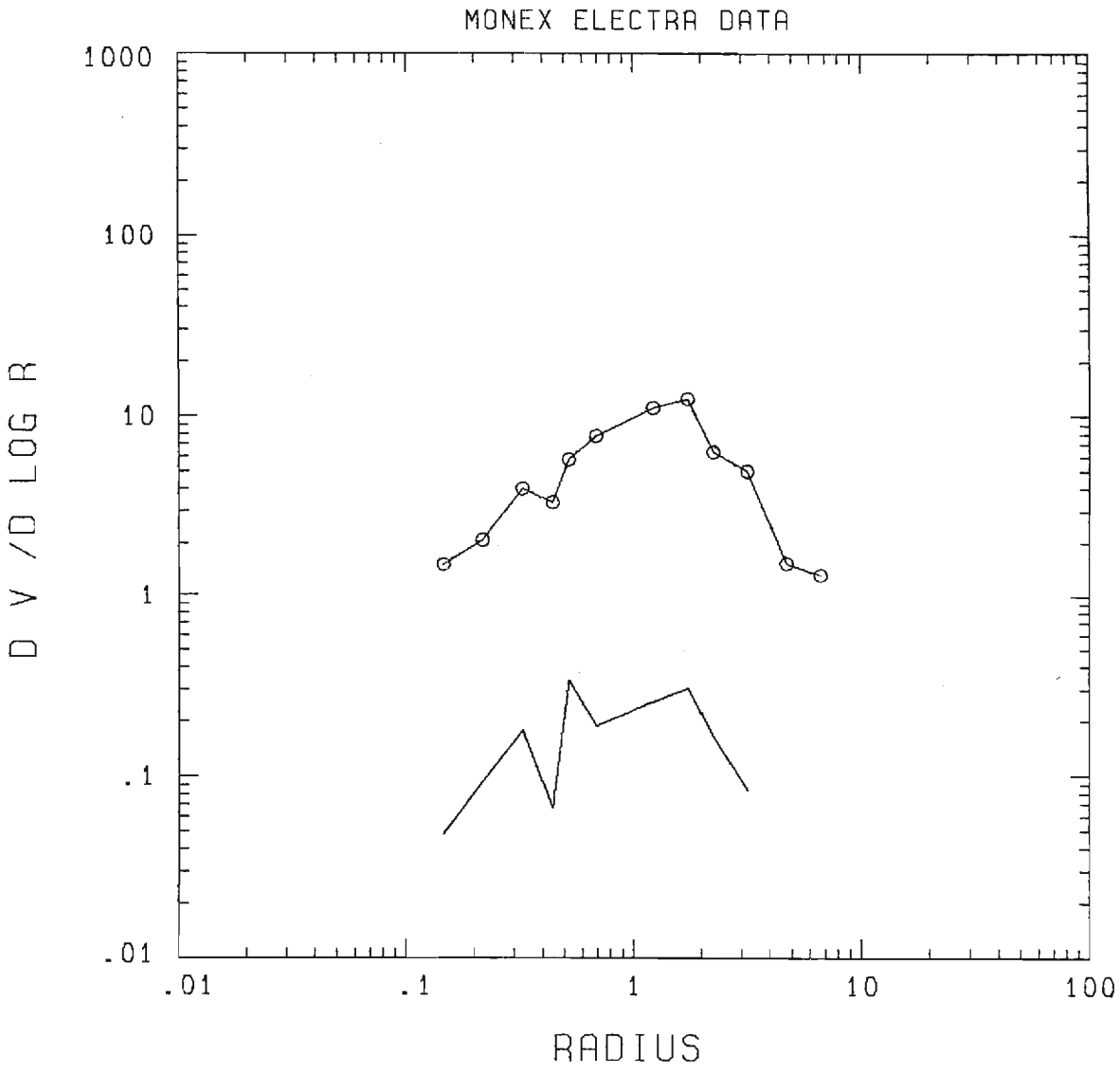
MONEX ELECTRA DATA
1000
100
10
1
.1
.01
D V /D LOG R
.01
.1
1
10
100
RADIUS

Fig. 6.

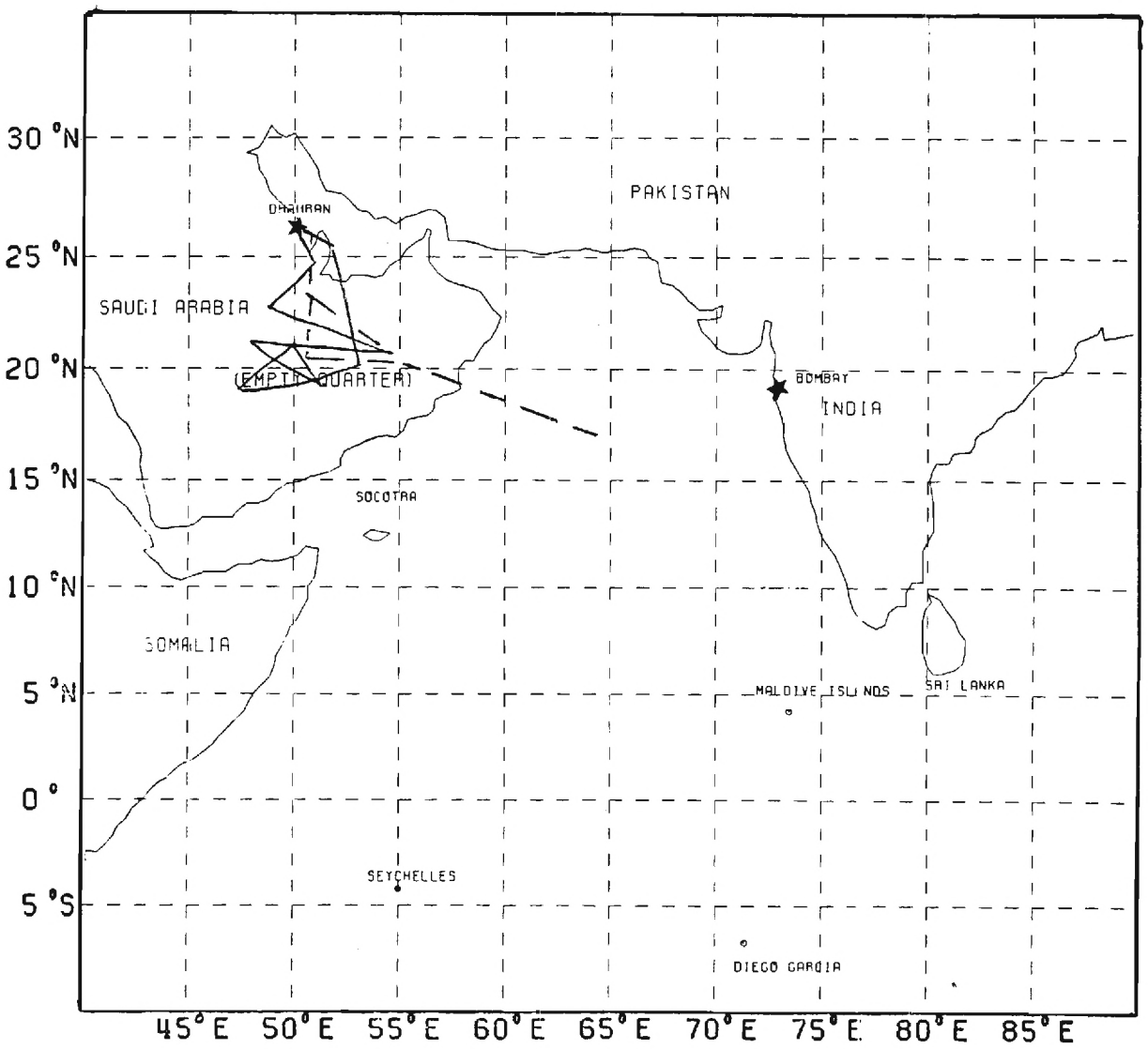
30 °N
25 °N
20 °N
15 °N
10 °N
5 °N
0 °
5 °S
45° E
50° E
55° E
60° E
65° E
70° E
75° E
80° E
85° E
PAKISTAN
DHAHRAN
SAUDI ARABIA
(EMPTY QUARTER)
BOMBAY
INDIA
SOCOTRA
SOMALIA
MALDIVE ISLANDS
SRI LANKA
SEYCHELLES
DIEGO GARCIA

Fig. 7.

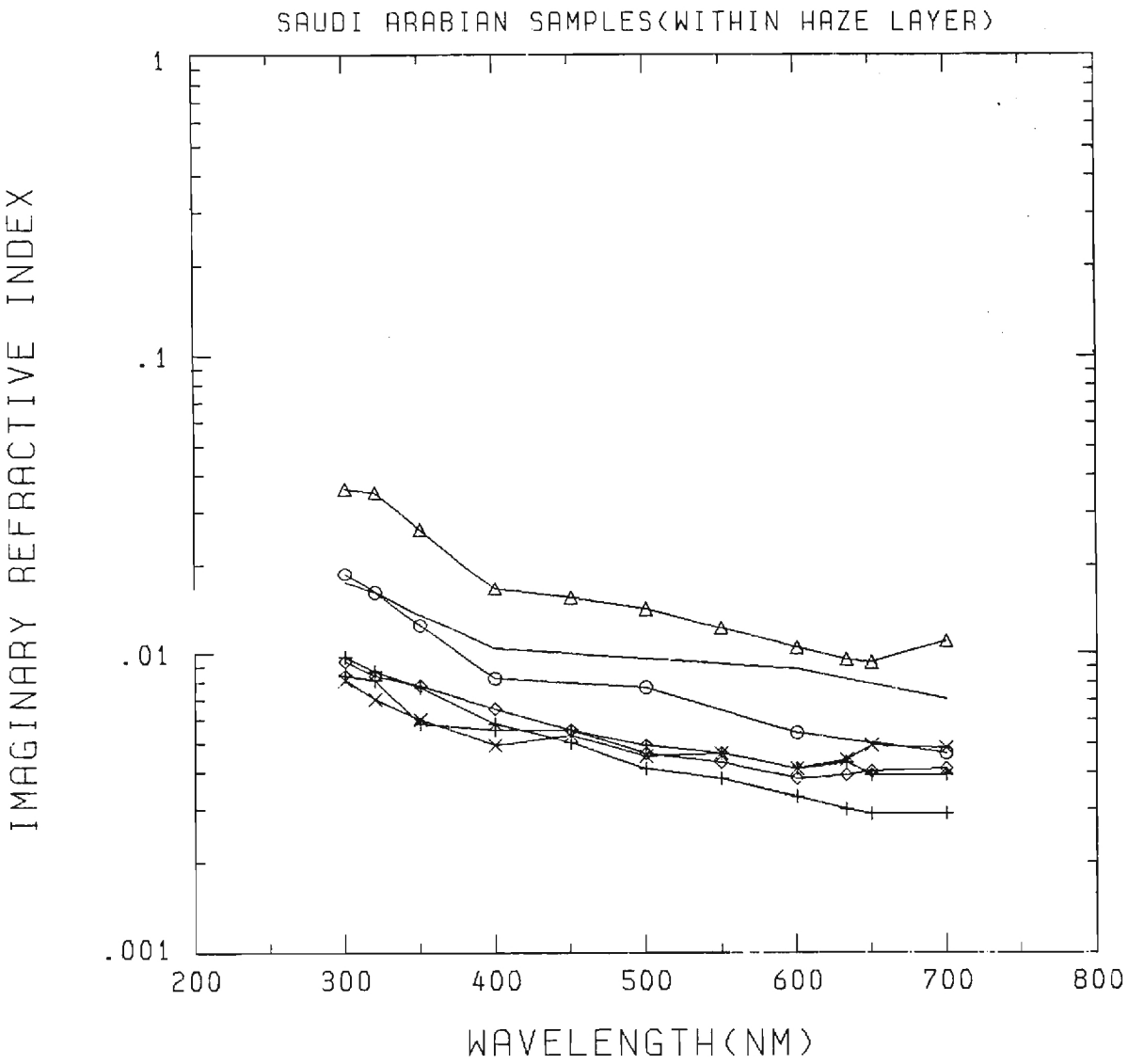
SAUDI ARABIAN SAMPLES(WITHIN HAZE LAYER)
IMAGINARY REFRACTIVE INDEX
1
.1
.01
.001
200
300
400
500
600
700
800
WAVELENGTH(NM)

Fig. 8.

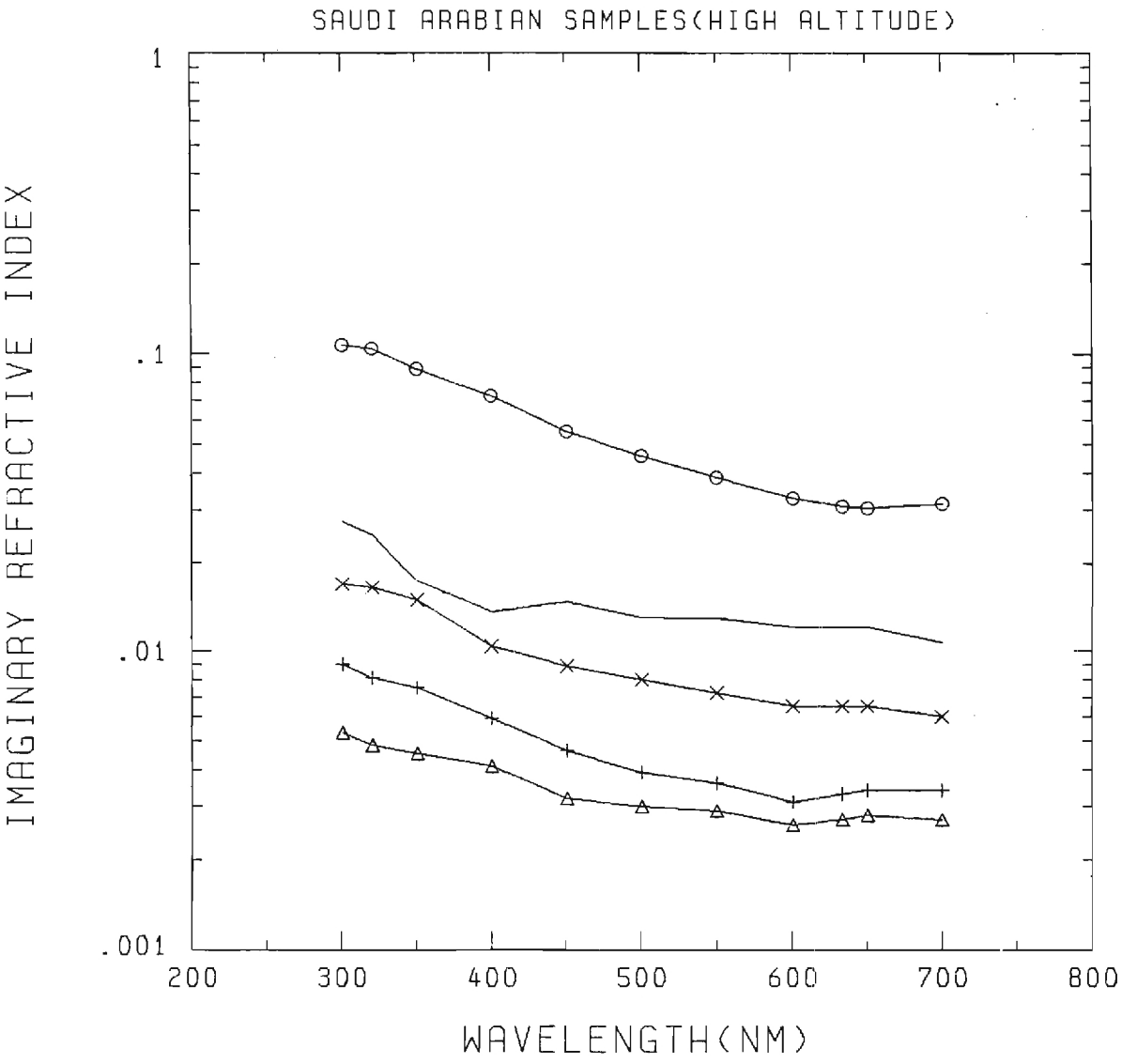
SAUDI ARABIAN SAMPLES(HIGH ALTITUDE)
IMAGINARY REFRACTIVE INDEX
1
.1
.01
.001
200
300
400
500
600
700
800
WAVELENGTH(NM)

Fig. 9.

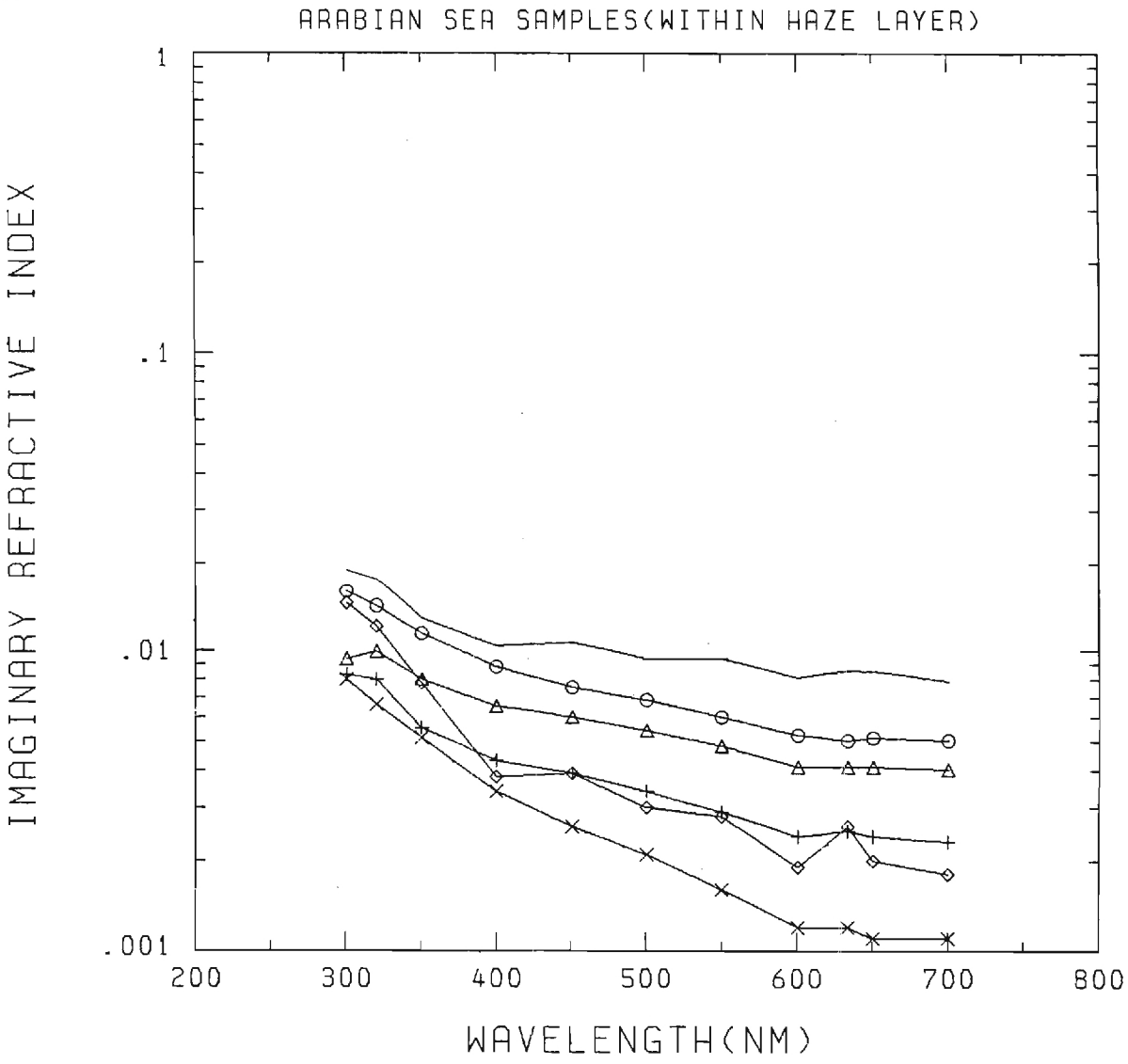
ARABIAN SEA SAMPLES(WITHIN HAZE LAYER)
IMAGINARY REFRACTIVE INDEX
1
.1
.01
.001
200
300
400
500
600
700
800
WAVELENGTH(NM)

Fig. 10.

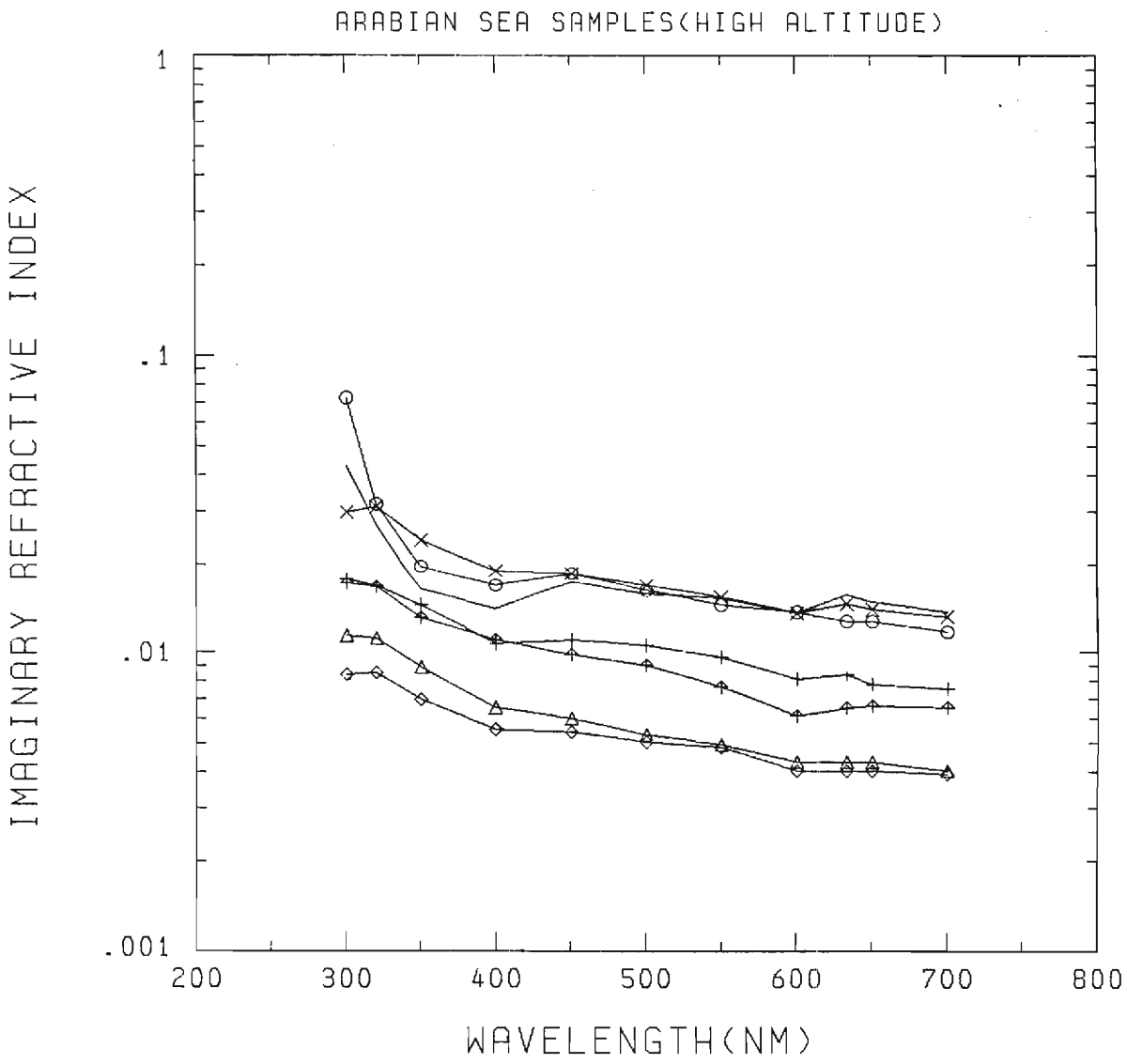
ARABIAN SEA SAMPLES(HIGH ALTITUDE)
IMAGINARY REFRACTIVE INDEX
1
.1
.01
.001
200
300
400
500
600
700
800
WAVELENGTH(NM)

Fig. 11.

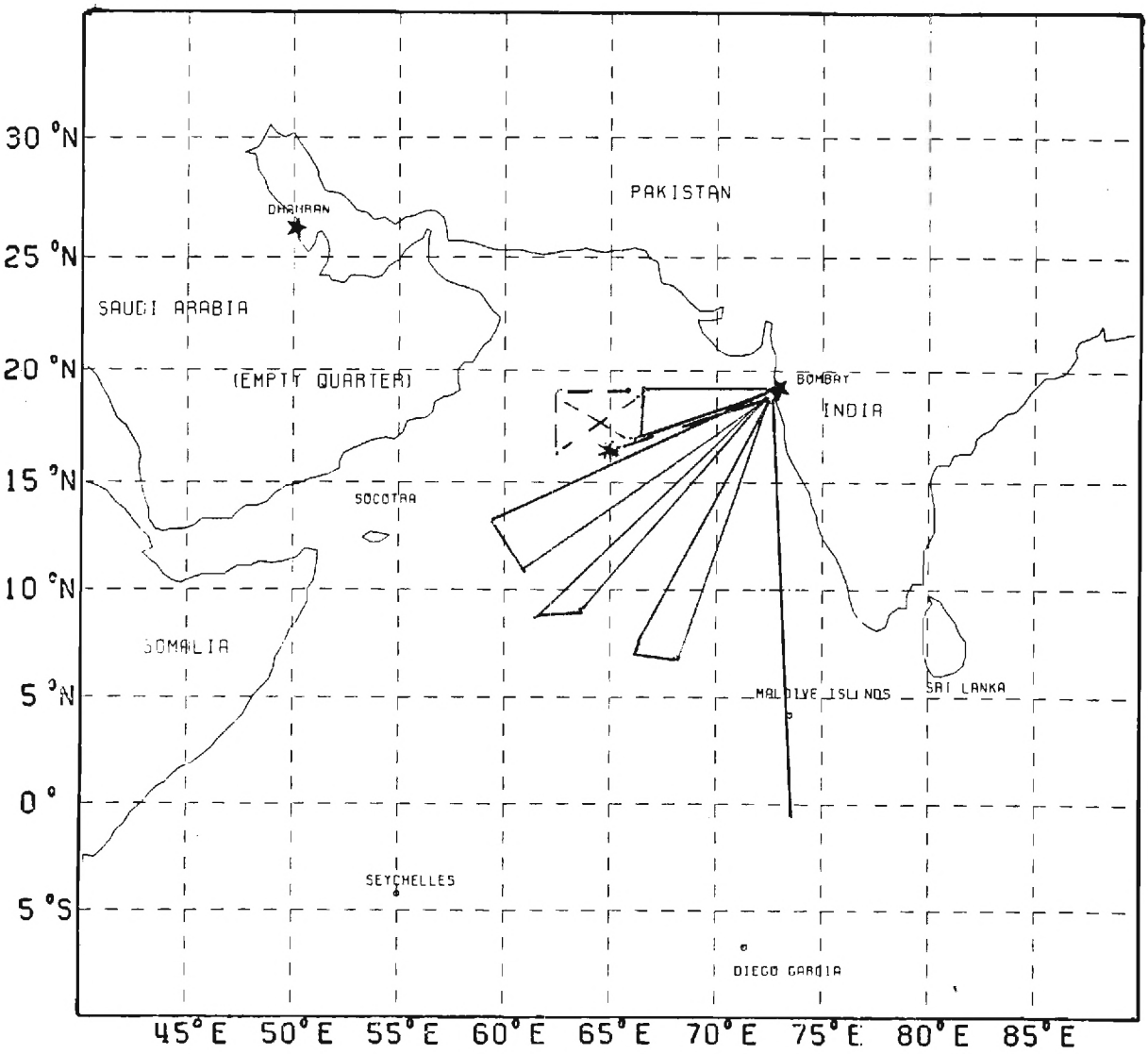
30 °N
25 °N
20 °N
15 °N
10 °N
5 °N
0 °
5 °S
45° E
50° E
55° E
60° E
65° E
70° E
75° E
80° E
85° E
PAKISTAN
DHAHRAN
SAUDI ARABIA
(EMPTY QUARTER)
BOMBAY
INDIA
SOCOTRA
SOMALIA
MALDIVE ISLANDS
SRI LANKA
SEYCHELLES
DIEGO GARCIA

Fig. 12.

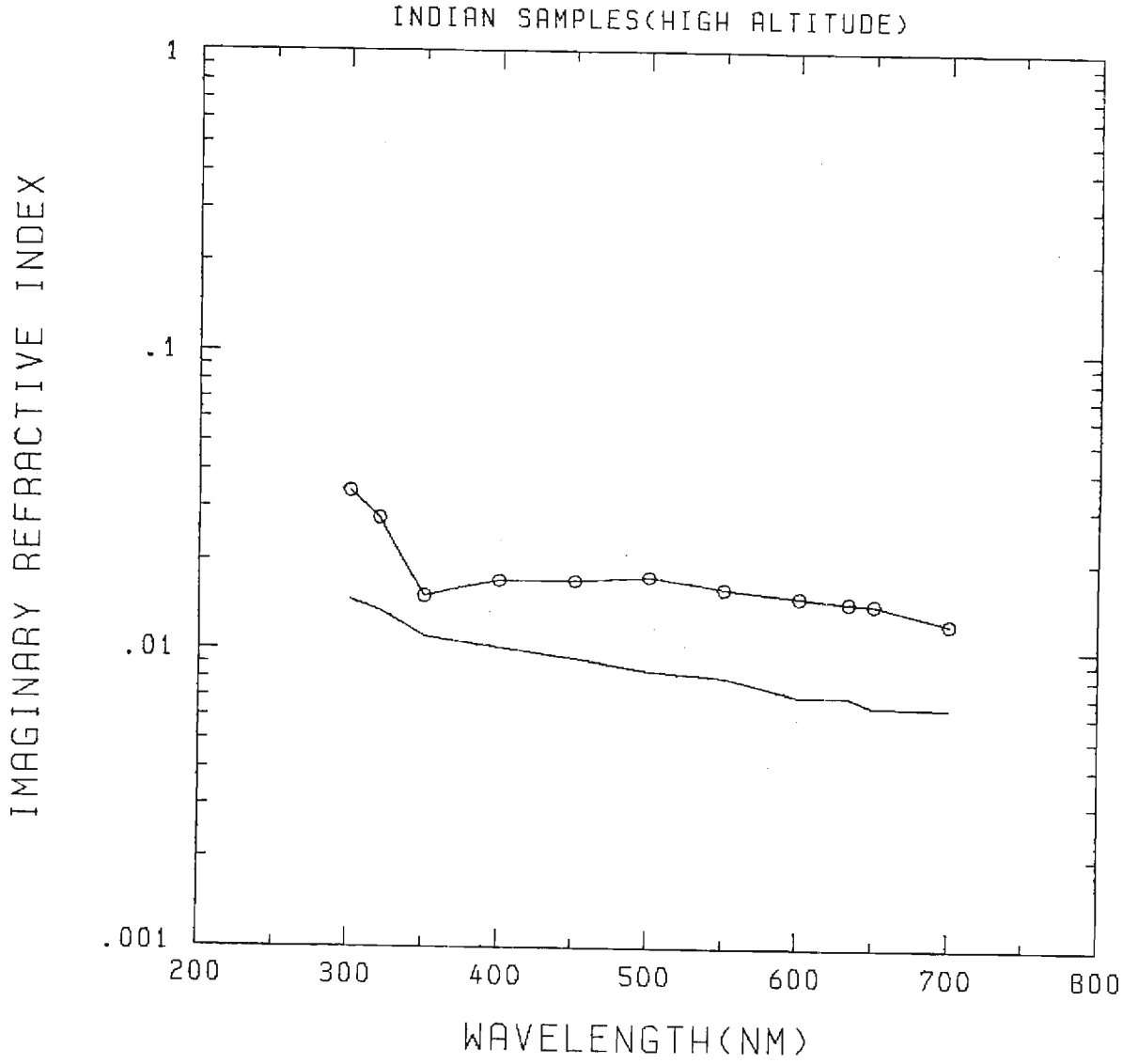
INDIAN SAMPLES(HIGH ALTITUDE)
IMAGINARY REFRACTIVE INDEX
1
.1
.01
.001
200
300
400
500
600
700
800
WAVELENGTH(NM)

Fig. 14.

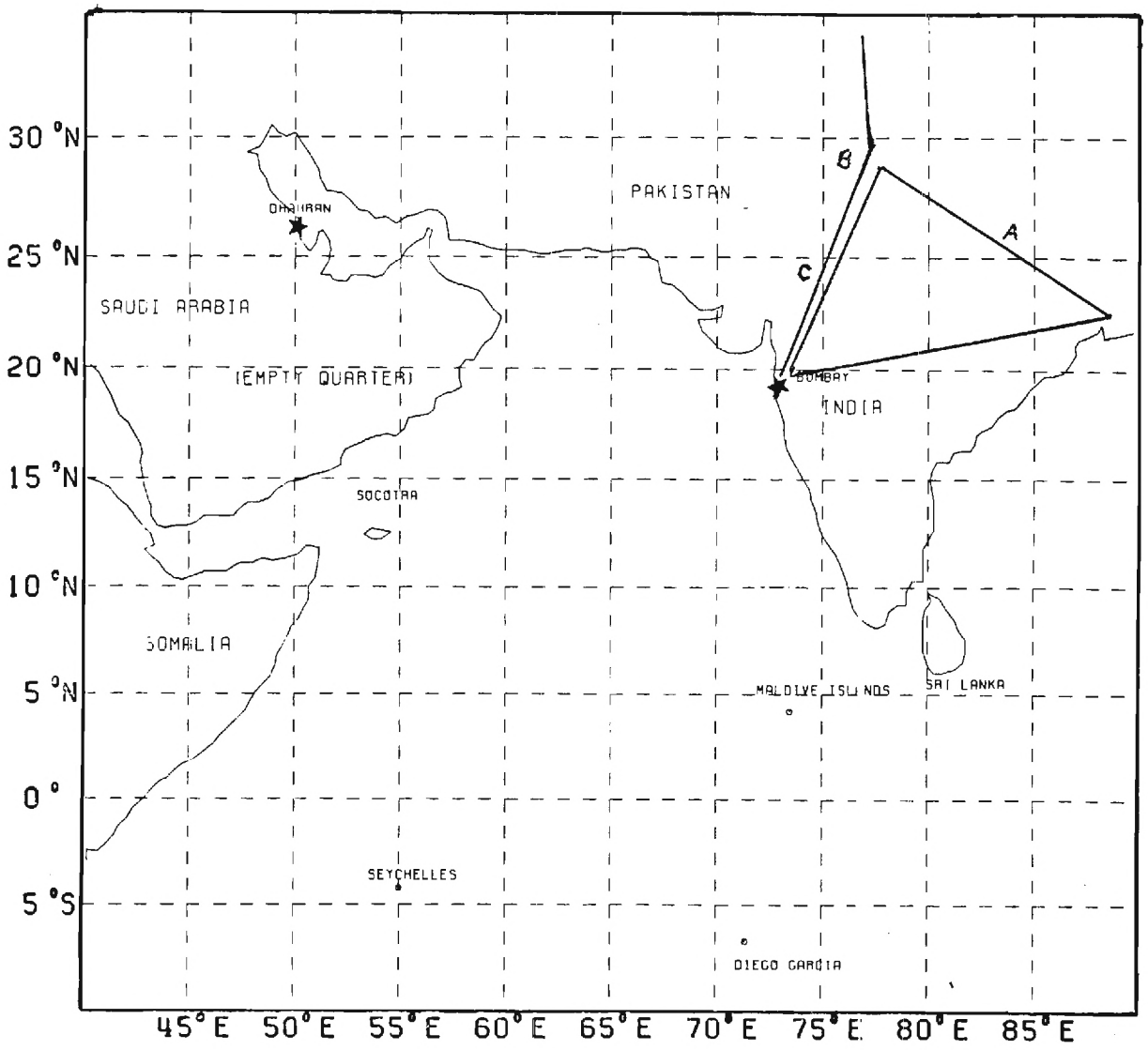
30 °N
25 °N
20 °N
15 °N
10 °N
5 °N
0 °
5 °S
45° E
50° E
55° E
60° E
65° E
70° E
75° E
80° E
85° E
PAKISTAN
SAUDI ARABIA
(EMPTY QUARTER)
INDIA
BOMBAY
SOCOTRA
SOMALIA
MALDIVE ISLANDS
SRI LANKA
SEYCHELLES
DIEGO GARCIA
A
B
C

Fig. 15.

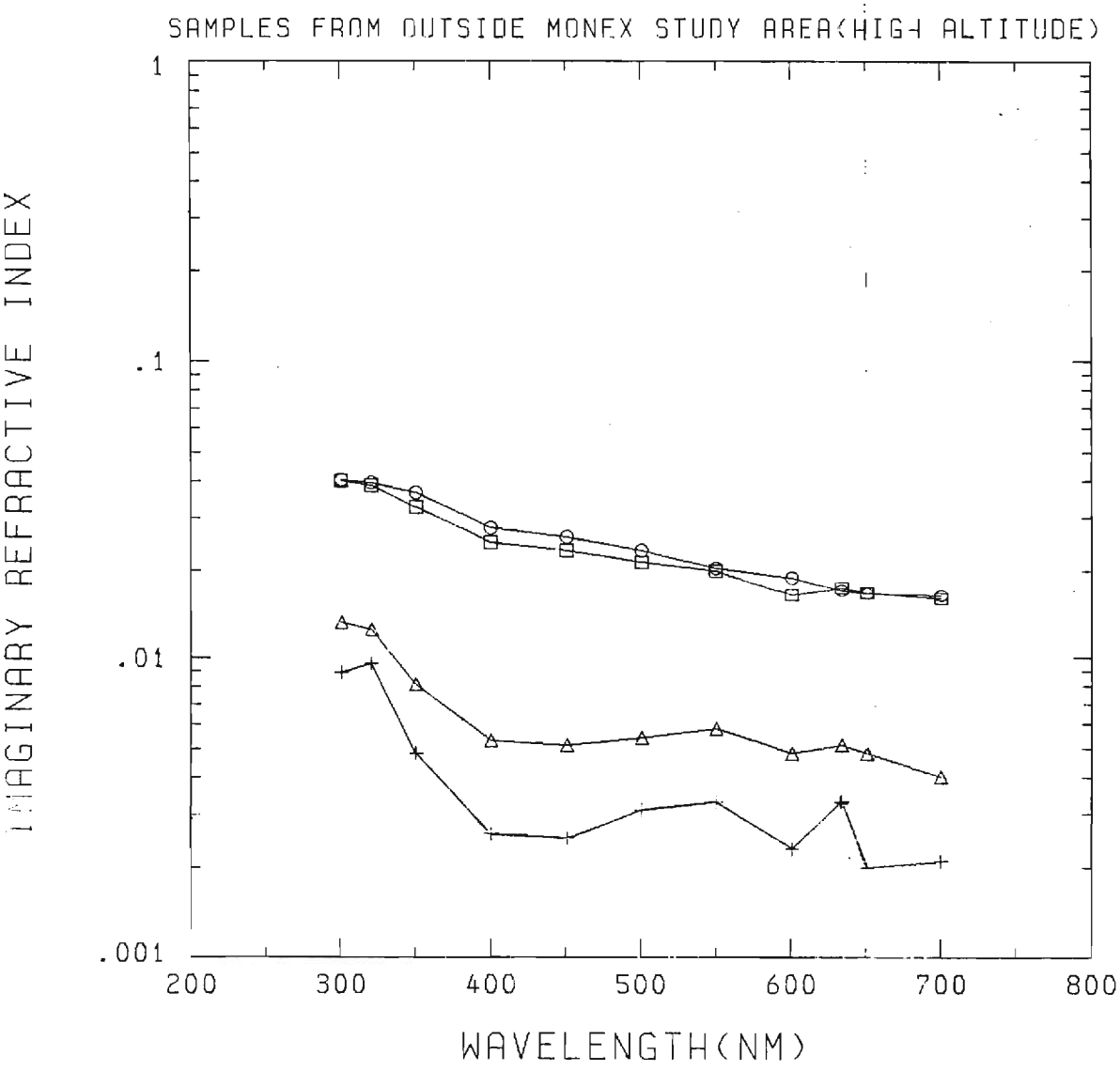
SAMPLES FROM OUTSIDE MONEX STUDY AREA(HIGH ALTITUDE)
IMAGINARY REFRACTIVE INDEX
1
.1
.01
.001
200
300
400
500
600
700
800
WAVELENGTH(NM)

Fig. 16.

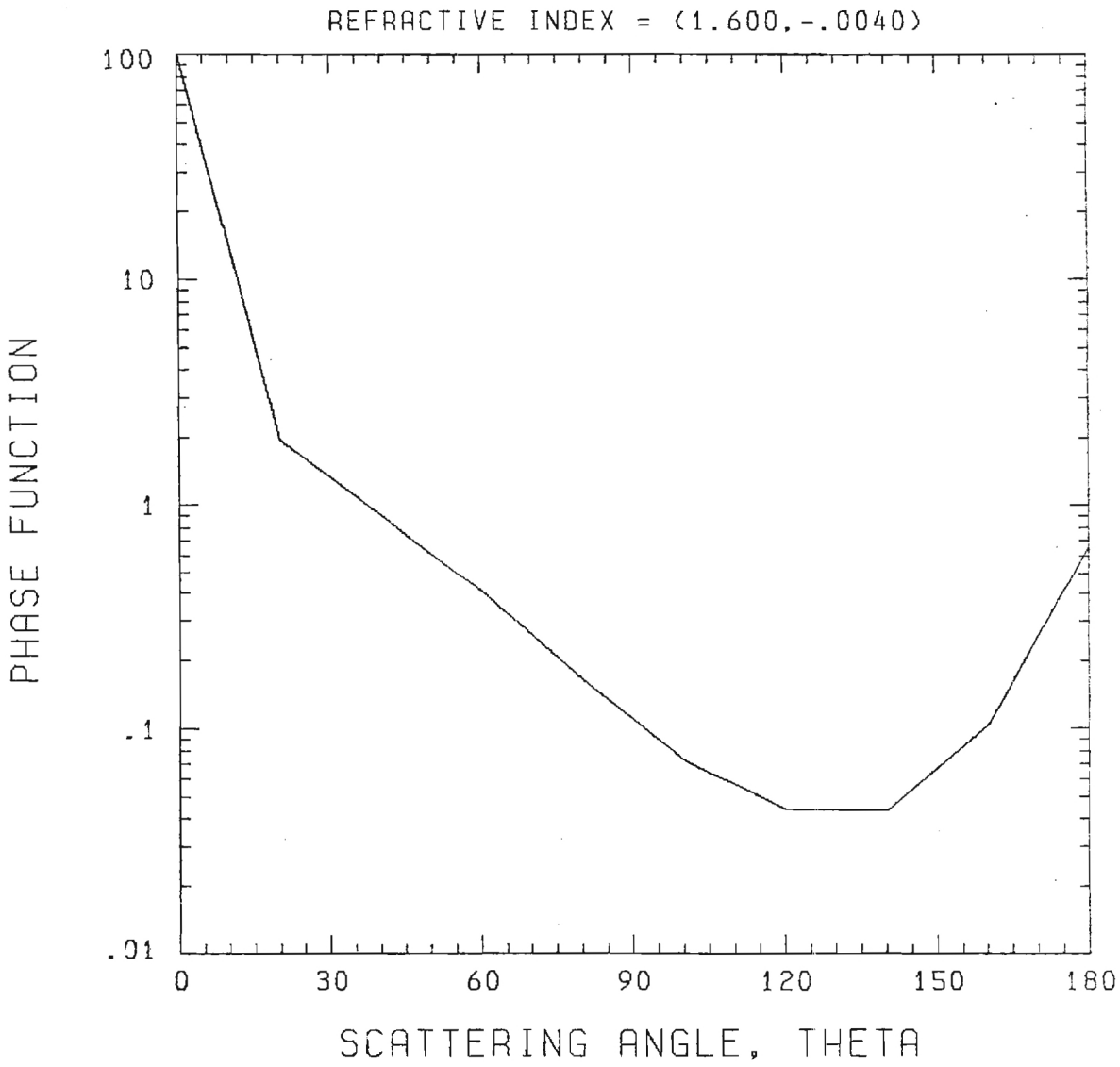

WAVELENGTH = .5500 MICRONS
EXTINCTION CROSS SECTION = .809E-06/CM
SCATTERING CROSS SECTION = .593E-06/CM

LOG-NORMAL SIZE DISTRIBUTION
RG = 2.6000 MICRONS
SG = 1.75
NP = .100E 01 PER CC

Fig. 17.

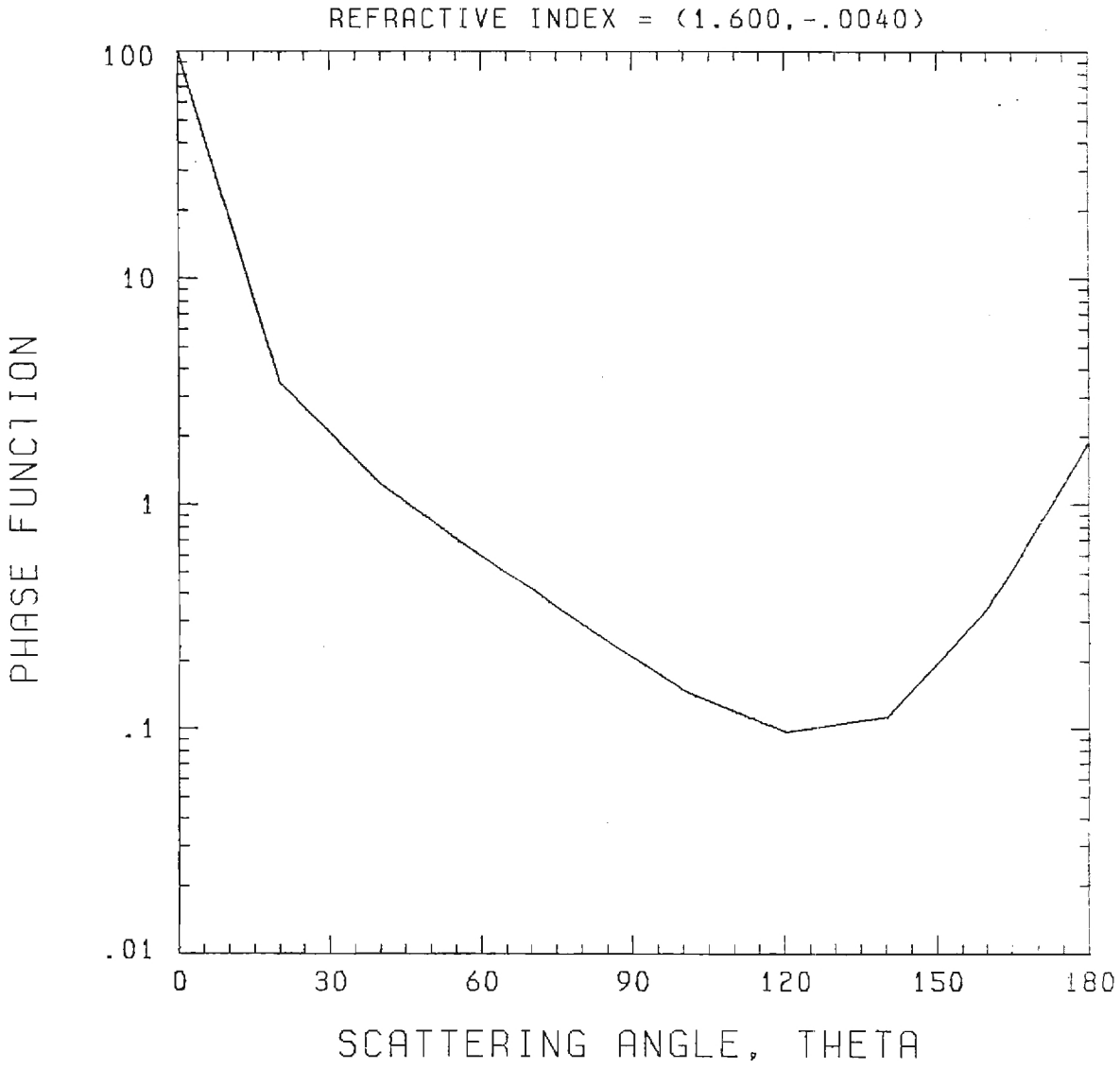

WAVELENGTH = .5500 MICRONS
EXTINCTION CROSS SECTION = .383E-07/CM
SCATTERING CROSS SECTION = .337E-07/CM

LOG-NORMAL SIZE DISTRIBUTION
RG = .4000 MICRONS
SG = 2.18
NP = .100E 01 PER CC

Fig. 18.

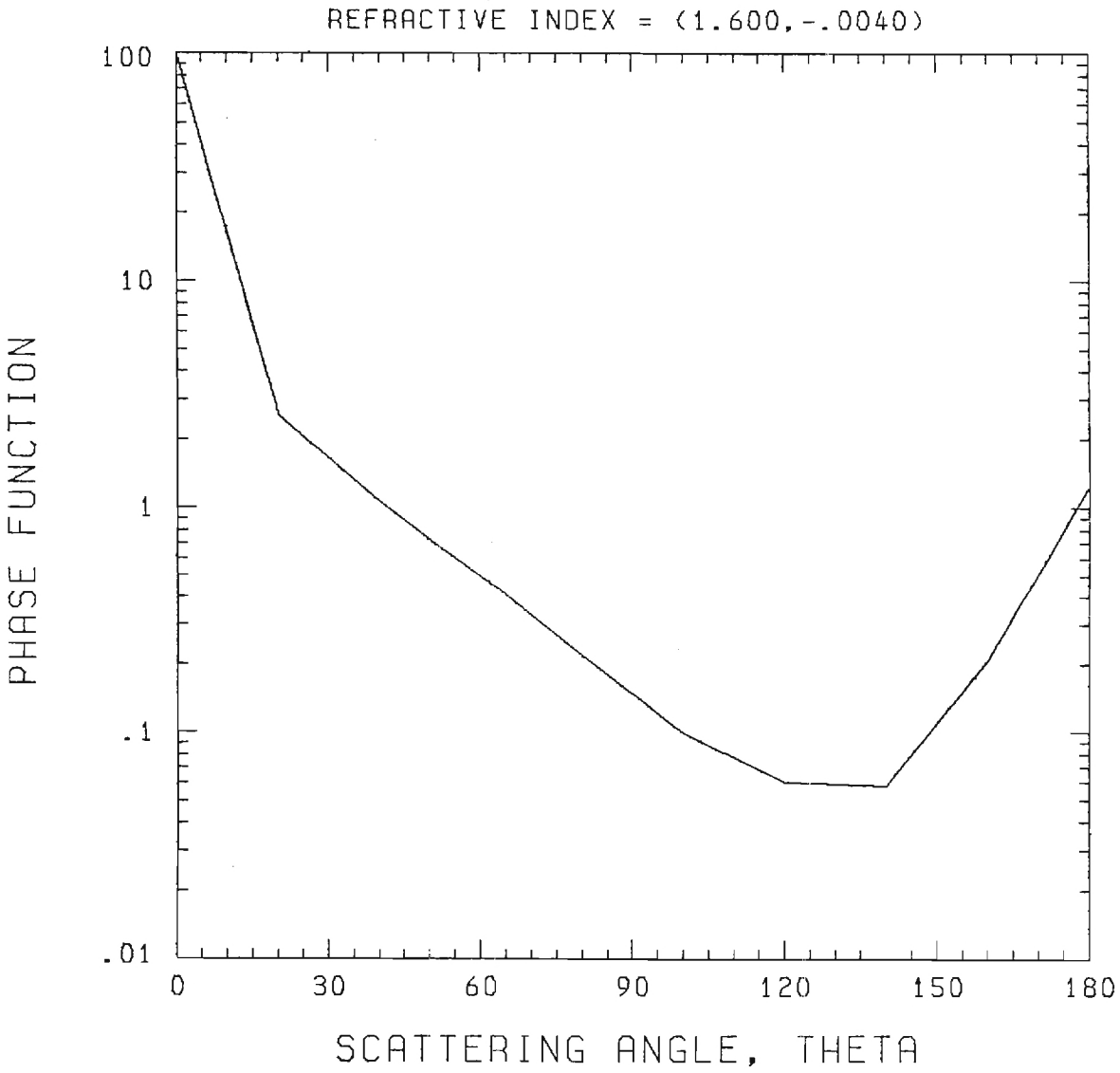

WAVELENGTH = .5500 MICRONS
EXTINCTION CROSS SECTION = .143E-06/CM
SCATTERING CROSS SECTION = .116E-06/CM

LOG-NORMAL SIZE DISTRIBUTION
RG = .8000 MICRONS
SG = 2.18
NP = .100E 01 PER CC

Fig. 19.

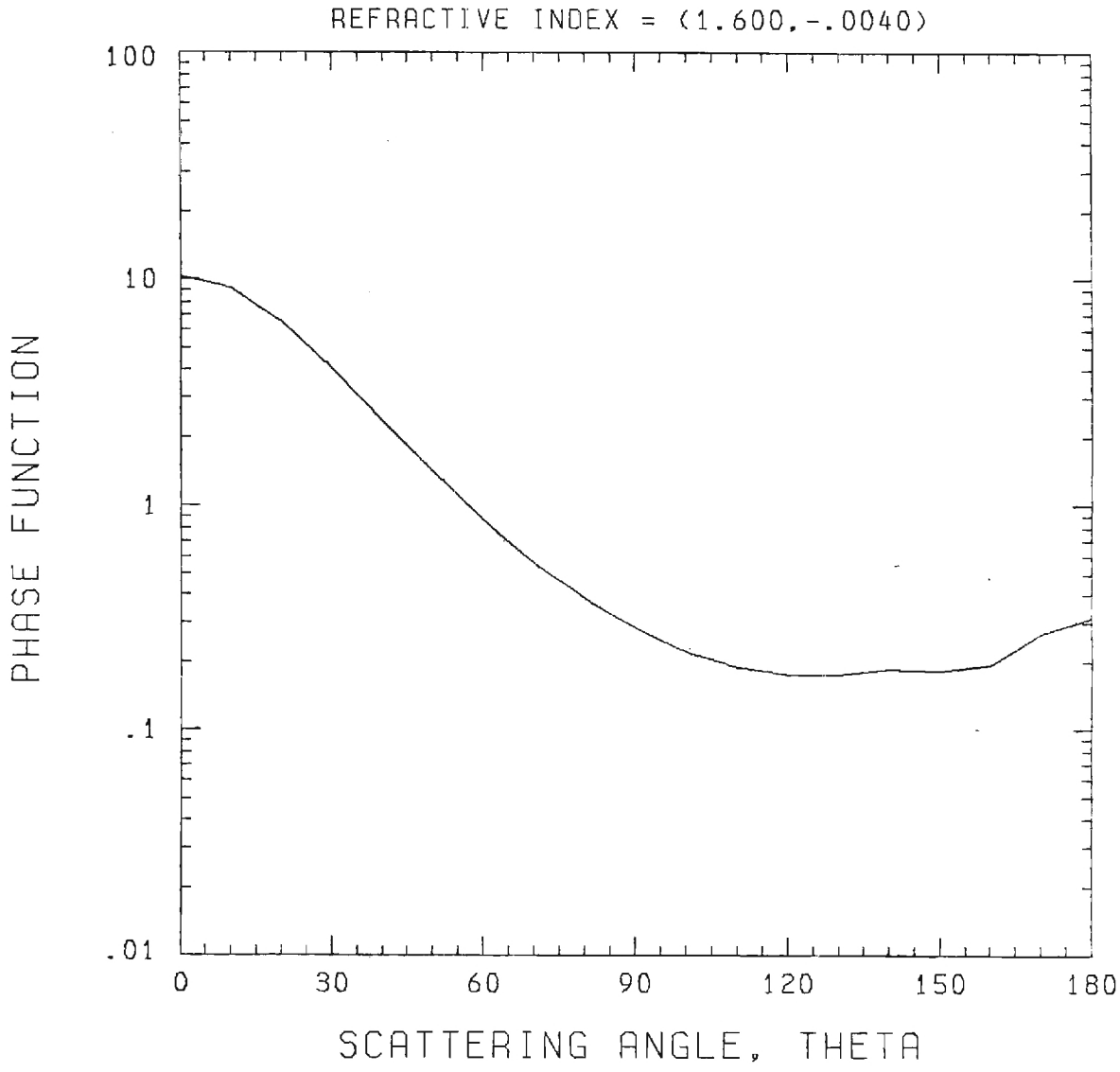

WAVELENGTH = .5500 MICRONS
EXTINCTION CROSS SECTION = .829E-06/CM
SCATTERING CROSS SECTION = .813E-06/CM

LOG-NORMAL SIZE DISTRIBUTION
RG = .1400 MICRONS
SG = 1.57
NP = .329E 03 PER CC

Fig. 20.

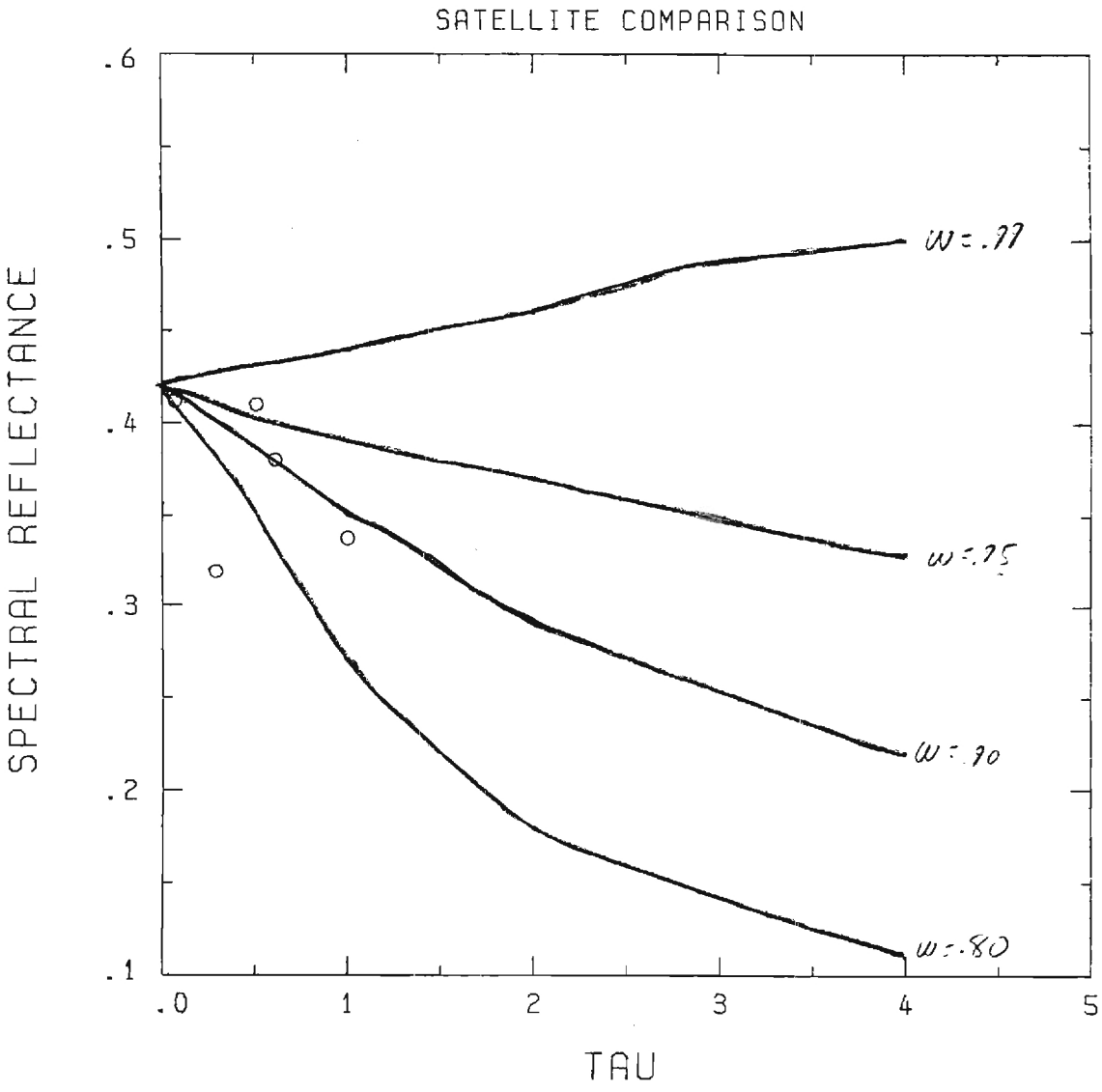
SATELLITE COMPARISON
SPECTRAL REFLECTANCE
.6
.5
.4
.3
.2
.1
.0
1
2
3
4
5
TAU
ω=.77
ω=.75
ω=.70
ω=.80

Fig. 21.

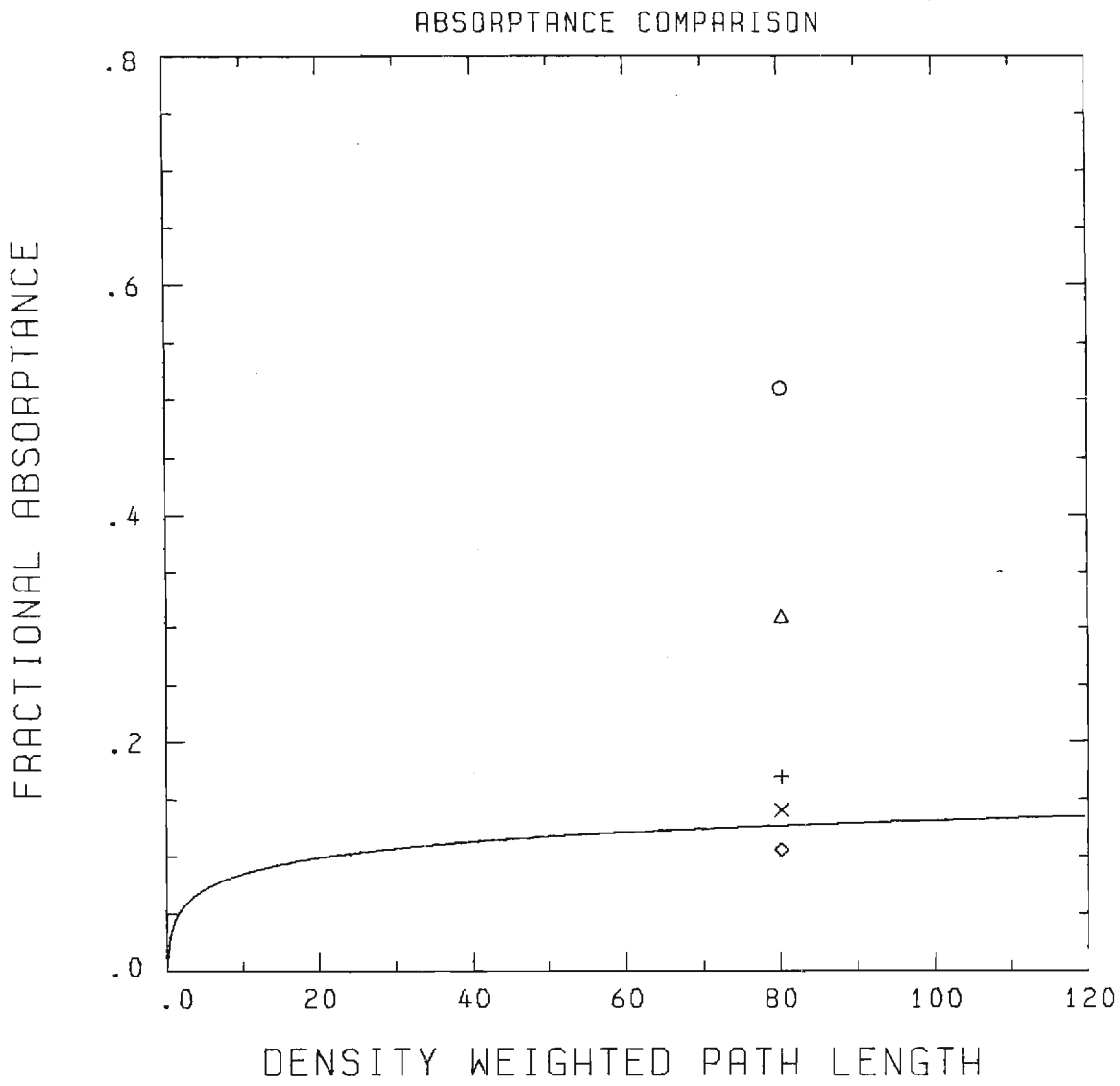
ABSORPTANCE COMPARISON
FRACTIONAL ABSORPTANCE
.8
.6
.4
.2
.0
.0
20
40
60
80
100
120
DENSITY WEIGHTED PATH LENGTH

Fig. 22.

APPENDIX A.

MONEX n_{IM} Data

Saudi Arabian Samples (Within Haze Layer)

λ(nm)	DF-1	DF-II	M-4	M-6	M-7	M-8	M-10
300	.0184	.0171	.0357	.0097	.0081	.0094	.0084
320	.0158	.0159	.0349	.0087	.0070	.0084	.0081
350	.0124	.0134	.0262	.0077	.0060	.0078	.0058
400	.0082	.0103	.0163	.0058	.0049	.0065	.0055
450	--	--	.0152	.0050	.0053	.0055	.0055
500	.0077	.0096	.0140	.0041	.0045	.0046	.0049
550	--	--	.0121	.0038	.0046	.0043	.0046
600	.0054	.0089	.0104	.0033	.0041	.0038	.0041
633	--	--	--	--	.0044	.0039	.0043
650	--	--	.0093	.0029	.0049	.0040	.0039
700	.0046	.0070	.0109	.0029	.0048	.0041	.0039

MONEX n_{IM} Data

Saudi Arabian Samples (High Altitude)

λ(nm)	M-3	M-5	M-9	M-11
300	.0273	.107	.0052	.0090
320	.0249	.1035	.0048	.0081
350	.0171	.0885	.0045	.0075
400	.0134	.0719	.0041	.0059
450	.0145	.0544	.0032	.0046
500	.0129	.0454	.0030	.0039
550	.0128	.0385	.0029	.0036
600	.0119	.0327	.0026	.0031
633	.0119	--	.0027	.0033
650	.0119	.0304	.0028	.0034
700	.0106	.0315	.0027	.0034

MONEX n_{IM} Data

Arabian Sea Samples (Within Haze Layer)

λ(nm)	M-14	M-E1	M-27	M-28	M-31	M-32
300	.0189	.0156	.0094	.0083	.0080	.0143
320	.0173	.0140	.0099	.0080	.0066	.0120
350	.0128	.0114	.0080	.0055	.0051	.0078
400	.0103	.0088	.0065	.0043	.0034	.0038
450	.0106	.0075	.0060	.0039	.0026	.0039
500	.0094	.0068	.0054	.0034	.0021	.0030
550	.0094	.0060	.0048	.0029	.0016	.0028
600	.0081	.0052	.0041	.0024	.0012	.0019
633	.0086	.0050	.0041	.0025	.0012	.0026
650	.0085	.0051	.0041	.0024	.0011	.0020
700	.0079	.0050	.0040	.0023	.0011	.0018

MONEX n_{IM} Samples

High Altitude Arabian Sea Samples

λ	M-13	M-15	M-22	M-23	M-24	M-25	M-26
300	.0426	.0721	.0113	.0174	.0298	.0084	.0169
320	.0270	.0316	.0111	.0165	.0309	.0085	.0164
350	.0161	.0195	.0089	.0143	.0240	.0069	.0130
400	.0139	.0166	.0065	.0106	.0188	.0055	.0109
450	.0171	.0185	.0060	.0109	.0185	.0054	.0098
500	.0155	.0160	.0053	.0105	.0166	.0050	.0090
550	.0150	.0143	.0049	.0096	.0151	.0048	.0076
600	.0134	.0135	.0043	.0081	.0134	.0040	.0061
633	.0154	.0126	.0043	.0084	.0144	.0040	.0065
650	.0146	.0126	.0043	.0078	.0138	.0040	.0066
700	.0135	.0116	.0040	.0075	.0131	.0039	.0065

MONEX n_{IM} Samples

Indian Samples (Within Haze Layer)

λ(nm)	M-17	M-18	M-20	M-21
300	.0210	.0079	.0058	.0122
320	.0191	.0070	.0048	.0110
350	.0145	.0053	.0045	.0092
400	.0131	.0039	.0040	.0066
450	.0121	.0034	.0033	.0057
500	.0110	.0031	.0030	.0047
550	.0101	.0029	.0031	.0044
600	.0084	.0026	.0028	.0038
633	.0085	.0028	.0029	--
650	.0086	.0028	.0033	.0037
700	.0083	.0028	.0033	.0038

MONEX n_{IM} Samples

Indian Samples (High Altitude)

λ(nm)	M-16	M-19
300	.0146	.0338
320	.0134	.0276
350	.0110	.0150
400	.0101	.0170
450	.0094	.0170
500	.0085	.0176
550	.0081	.0160
600	.0070	.0150
633	.0070	.0145
650	.0065	.0143
700	.0064	.0123

MONEX n_{IM} Samples

Samples from Outside of MONEX Study Area (High Altitude)

λ(nm)	M-1	M-2	M-35	M-37
300	.0369	.0400	.0131	.0089
320	.0384	.0391	.0124	.0095
350	.0325	.0362	.0081	.0048
400	.0249	.0277	.0053	.0026
450	.0234	.0258	.0051	.0025
500	.0213	.0234	.0054	.0031
550	.0199	.0203	.0058	.0033
600	.0163	.0189	.0048	.0023
633	.0173	--	.0051	.0033
650	.0166	.0165	.0048	.0020
700	.0158	.0163	.0040	.0021